PHYSICAL REVIEW A **79**, 012703 (2009)

Resonance asymmetry and external field effects in the photorecombination of Ti^{4+}

D. Nikolić and T. W. Gorczyca
Western Michigan University, Kalamazoo, Michigan 49008, USA

N. R. Badnell
University of Strathclyde, Glasgow G4 0NG, United Kingdom

(Received 23 August 2008; published 9 January 2009)

We report on multiconfiguration Breit-Pauli calculations for the photorecombination of Ti^{4+} ions. Through a detailed comparison with the Test Storage Ring measurements of Schippers *et al.*, we quantify the interference effects for the broad, asymmetric, near-threshold, highly correlated $3p^5 3d^2(^2F)$ resonances. We also discuss the enhanced field ionization effects on recombined $3p^6 n\ell$ Rydberg states. This is due to the perturbation of the below-threshold tails of two of the broad $3p^5 3d^2(^2F)$ resonances, giving rise to a "forced autoionization" phenomenon, increasing the field ionization effects. By accounting for interference for the lowest $n=3,4$ resonances, and field effects as $n \rightarrow \infty$, excellent agreement between our computed results and the experimental photorecombination spectrum is obtained.

DOI: 10.1103/PhysRevA.79.012703 PACS number(s): 34.80.Lx

I. INTRODUCTION

The modeling of nonequilibrium laboratory and astrophysical plasmas requires accurate recombination cross sections. For example, the use of titanium metal films deposited on a carbon divertor, in order to reduce its erosion rate, requires the knowledge of the excitation cross sections for titanium as an impurity in tokamak plasmas [1]. From an astrophysical perspective, due to their nuclear stability, ions of transition elements in the fourth row of the Periodic Table are often found in spectra of supernova remnants such as Cassiopeia A [2], where the abundance of ^{44}Ti serves as a probe for nucleosynthesis.

The burgeoning interest in atomic structure of low-charged Ti ions [3–15], particularly inner-shell excitation followed by autoionization [16–28], revealed that the description of resonances in Ti^{3+} can be surprisingly difficult. This is also the case in dielectronic recombination (DR) of highly charged ions, such as $^{207}Pb^{53+}$ and $^{208}Pb^{53+}$ [29], where isotope effects may open or close the DR channels by shifting low-energy resonances above or below threshold. Furthermore, a recent measurement [30] of the Fe^{13+} recombination rate coefficient indicated the need for improved data in the temperature range where these ions form in photoionized plasmas.

To address the need for accurate DR data, we have embarked on a research program to compute DR cross sections for all ions of astrophysical interest [31]. To date, results have been reported for all elements up through zinc for the isoelectronic sequences ranging from H-like to Mg-like [32–43]. Good agreement between theoretical results and experimental measurements, at the Test Storage Ring (TSR) in Heidelberg, have been obtained within the experimental uncertainty of 20% for most sequences. However, on progressing into the *M* shell, theory does not compare as favorably with experiment. This is most likely due to the more demanding atomic structure associated with third-row systems for which the highly correlated $3p$ and $3d$ subshells can now be populated. Because of the need for a more complex atomic structure treatment, and following benchmark calculations [44,45] for iron ions with partially filled *M* shell, this work aims to address DR of Ti^{4+} for which storage ring experimental results also exist [24].

The more general photorecombination (PR) process consists of the coherent contributions from resonant DR and direct radiative recombination (RR). This is of considerable importance for PR of Sc^{3+} and Ti^{4+} in that the existence of two very broad asymmetric $3p^5 3d^2(^2F^\circ_{5/2,7/2})$ resonances had been theoretically established [46,47] and experimentally unveiled in the near-threshold region [24,48]. Those findings present the impetus for this work and a special challenge when using our multiconfiguration Breit-Pauli (MCBP) method, as generally used for DR computations [49], since interference effects between resonant and direct coherent pathways are neglected in the lowest-order, computationally efficient mode.

For the near-threshold region, a less-efficient next-highest-order perturbative approach [46] is used. This has the advantage of treating nonperturbatively all interference effects for the low-lying broad resonances. From earlier PR work on Sc^{3+} [46,48,50–53], it is well established that for low-charged Ar-like ions, there exist broad, asymmetric, highly correlated, near-threshold $3p^5 3d^2(^2F^\circ_J)$ resonances that deserve special theoretical attention. For the higher-energy DR computations, where numerous Rydberg series of narrow, noninterfering resonances prevail, we use the lower-order, highly efficient AUTOSTRUCTURE program [49]. Thus both an adequate description of the low-energy interfering-resonance region and an efficient method for treating the Rydberg limits, with additional consideration of external electric field effects, is obtained.

The rest of the paper is organized as follows. We first address the computational approaches in Sec. II, and present the atomic structure for Ti^{4+} and Ti^{3+}. Next, we analyze the available experimental data in Sec. III, and describe a deconvolution method for inferring the PR cross section from the experimental rate coefficient. Near-threshold recombination spectra and the complete Rydberg series are compared to the latest experimental and other theoretical studies in Sec. IV, and a brief summary follows in Sec. V.

II. THEORETICAL METHODOLOGY

The perturbative method used in our present study neglects higher-order effects such as resonance-background (the background being RR) and resonance-resonance interferences [54], which in turn has the advantage of analytically averaging the resonant recombination pathways of entire Rydberg series [55]. This implementation is commonly referred to the independent-processes isolated-resonance distorted-wave (IPIRDW) approximation, where both electron-electron and electron-photon interactions are treated to first order. We have assessed that this is a reliable approximation except in rare cases such as the broad, highly correlated $3p^5 3d^2(^2F^{\circ})$ resonances. Nonetheless, in a many-body third-order perturbative study of low-lying resonances in PR cross sections of highly charged uranium ions, Pindzola, *et al.* [56] demonstrated that even though resonance-background interference effects are not evident in the total DR cross section, they are present in partial DR cross sections and thus observable [57] in high-resolution x-ray spectra associated with the recombination event [58]. Therefore we complement our investigation of the near-threshold resonance region with a higher-order perturbative approach.

A. Processes of interest

The specific PR processes of interest are the following:

$$\begin{array}{lcl} e^- + \mathrm{Ti}^{4+}(3p^6) & \rightarrow & \mathrm{Ti}^{3+**}\begin{pmatrix} 3p^5 3dn\ell \\ 3p^5 4sn\ell \end{pmatrix} \\ & & \mathrm{DR}\ \downarrow \\ & \mathrm{RR}\searrow & \\ & & \mathrm{Ti}^{3+*}(3p^6 n\ell) + \hbar\omega, \end{array} \tag{1}$$

where an initial electron incident upon a Ti^{4+} target ion (forming a continuum state c) is either directly captured via RR into a Ti^{3+*} bound state b or captured into a doubly excited Ti^{3+**} autoionizing resonance state d. This intermediate state then decays radiatively to the same final bound state b, completing the PR process. It is customary to denote the Ti^{4+} target states as N-electron states, and the Ti^{3+} bound, resonance, and electron-plus-ion scattering states as $(N+1)$-electron states. The present work investigates DR resonances formed by inelastic single-electron $(3p \rightarrow 3d, 4s)$ excitations from the Ti^{4+} ground state, giving rise to 16 Rydberg series of intermediate autoionizing $3p^5 3dn\ell$ and $3p^5 4sn\ell$ states. The incoherent partial-wave contributions for each $J\pi$ in Eq. (1) can be described as

$$\begin{array}{lcl} [e^- + 3p^6]_{J,\pi=\mathrm{odd}} & \rightarrow & \begin{bmatrix} 3p^5(3dn\ell) \\ 3p^5(4sn\ell) \end{bmatrix}_{J,\pi=\mathrm{odd}} \\ & \searrow & \downarrow \\ & & [3p^6 3d]_{3/2,5/2}. \end{array} \tag{2}$$

At this point we note that, quantum mechanically, the transitions in Eq. (2), through different resonances d and/or the direct continua c, to the same final bound state b, constitute coherent pathways and therefore interference effects may arise. While such cases are rare in PR [55,59], we have predicted theoretically [46,47] that the $3p^5 3d^2(^2F^{\circ})$ resonances formed in Sc^{2+} and Ti^{3+} exhibit asymmetric features associated with resonance-background and/or resonance-resonance interference effects.

To handle this particular case of $n\ell = 3d$, where these resonances occur in the near-threshold region, we extend our usual MCBP calculations at lowest order to include next-highest order interference effects.

B. Theoretical treatment of PR

For the treatment of the entire PR process as a function of the electron's center-of-mass (c.m.) energy ϵ, we resort to the well-established IPIRDW approximation, as is usually invoked in the operative mode of the AUTOSTRUCTURE atomic code [49] and other codes [60,61]. Here we outline only the main operative expressions for DR cross sections within an IPIRDW framework; details may be found elsewhere [44]. A key advantage of the IPIRDW approach is that its independent-processes aspect allows the separation of the photorecombination cross section σ^{PR} into nonresonant σ^{RR} and resonant σ^{DR} contributions. The isolated-resonances aspect offers a further simplification of resonant contributions to σ^{DR} that can be calculated as an incoherent sum over all bound and resonant states,

$$\epsilon\sigma^{\mathrm{DR}}(\epsilon) = \frac{2}{\pi}\sum_b \sum_d \frac{\mathcal{S}^d_{c\rightarrow b}/\bar{\Gamma}_d}{1+\varepsilon_d^2}, \tag{3}$$

with reduced c.m. energy $\varepsilon_d = 2(\epsilon - \epsilon_d)/\bar{\Gamma}_d$ and (partial) integrated resonant strength

$$\mathcal{S}^d_{c\rightarrow b} = 4.95 \times 10^{-12}[\mathrm{Mb\ eV^2\ s}] \times \frac{g_d}{2g_{ion}} \frac{A^a_{d\rightarrow c}A^r_{d\rightarrow b}}{\sum_{c'}A^a_{d\rightarrow c'} + \sum_s A^r_{d\rightarrow s}}. \tag{4}$$

Here g_d and g_{ion} are the statistical weights of the resonance and final ionic states, respectively, and the summation indices c' and s in Eq. (4) run over all states that are attainable from a given resonant state d either by autoionization or by radiative decay. Hence a sum over c' accounts for resonant scattering (excitation) and gives the total autoionization rate A^a_d. The sum over s includes not only bound states that are below the $\mathrm{Ti}^{4+}3p^6$ first ionization limit $E^{(1)}_{th}$, but also may consider radiative cascade through other autoionizing states, giving the total radiative rate A^r_d.

The partial autoionization rates, $A^a_{d\rightarrow c}$, are computed using an energy-normalized distorted wave coupled to a target wave function to represent the continuum wave function $|c\rangle$, and a bound-state wave function for the resonance $|d\rangle$, yielding an autoionization rate, according to Fermi's Golden Rule [62], as

$$A^a_{d\rightarrow c} = 2\pi|\langle c|\mathbb{V}|d\rangle|^2, \tag{5}$$

where $\mathbb{V} = \sum_{j>i}\frac{1}{r_{ij}}$ represents the electron-electron interaction operator. Likewise, the spontaneous radiative decay rate of the resonance state $|d\rangle$ to a bound state $|b\rangle$ is given by

$$A^r_{d\to b} = \frac{4}{3}\alpha^3\omega^3_{d\to b}|\langle b|\mathbb{R}|d\rangle|^2, \tag{6}$$

with photon energy $\omega_{d\to b}$, fine-structure constant α, and electric-dipole moment $\mathbb{R}=\Sigma_i r_i$ in atomic units. In order to directly compare our theoretical results with experimental results [24], Eqs. (3) and (4) implicitly assume that both the resonance position, $\epsilon_d = E_d - E^{(1)}_{th}$, and the total width, $\bar{\Gamma}_d = \hbar(A^a_d + A^r_d)$, are in units of eV. In addition, the summation index d in Eq. (3) runs over resonant states, given in Eq. (1) for $3 \leqslant n \leqslant 1000$ and $0 \leqslant \ell \leqslant 10$, whereas the index b covers all true bound states, omitting radiatively decayed states that subsequently reionize due to the motional Stark effect; this is discussed more fully in Sec. IV C 1. The use of the IPIRDW approximation has the further advantage of easily mapping-out and analytically integrating the numerous narrow resonance profiles.

Additional formulas that are often needed for comparison with other data are relations, in the length gauge, among the radiative transition rate $A^r_{u\to l}$, the line strength S, and the oscillator strength f:

$$A^r_{u\to l}[\mathrm{ns}^{-1}] = 32.1298\Delta E^2_{ul}\frac{g_l}{g_u}f, \tag{7}$$

$$f = \frac{2\Delta E_{ul}}{3g_l}S; \tag{8}$$

with the energy difference ΔE_{ul} and line strength S in atomic units, and statistical weights g_u and g_l of the upper and lower states, respectively.

However, from previous investigations of Sc^{3+} and Ti^{4+} [12,24,46–48,50–53], we anticipate the existence of very broad, strong resonances near the $3p^6$ threshold for which this efficient approximation is no longer valid, and so we first discuss the more general, unified theory of photorecombination, followed by the simplified IPIRDW approximation.

C. Interference effects in the PR cross section

For near-threshold energies $\epsilon \lesssim 1.85$ eV, it is necessary to consider the unified process of an incident electron wave $\epsilon_{\ell,J}$ upon the Ti^{4+} $3p^6(^1S_0)$ target state, comprising an initial continuum $|c\rangle$, that can either be (i) directly captured into the ground state $3p^63d$ of Ti^{3+}, or (ii) dielectronically captured (with rate equal to the inverse autoionization rate $A^a_{d\to c}$) to intermediate autoionizing states $|d\rangle = \{3p^53d^2, 3p^53d4s\}$, followed by radiative decay to bound states $|b\rangle$ of Ti^{3+}. This is schematically illustrated in Fig. 1 and can be represented as

$$\begin{array}{ccl} e^- + \mathrm{Ti}^{3+} = |c\rangle & \leftrightarrow & |d\rangle = \mathrm{Ti}^{3+**}(3p^53d^2, 3p^53d4s) \\ & \searrow & \downarrow \\ & & |b\rangle = \mathrm{Ti}^{3+*}(3p^63d) + \hbar\omega. \end{array}$$

Here we have determined theoretically (see Sec. IV) that seven resonances exist. The two $3p^53d^2(^2F^\circ_{5/2,7/2})$ resonances, labeled as $d_{1,2}$, are broad, asymmetric, highly correlated, and straddle the first ionization limit $E^{(1)}_{th}$. The remaining five $3p^53d4s$ resonances consist of the two doublets $^2P^\circ_{1/2,3/2}$, labeled as $d_{3,4}$, and the three quartets $^4P^\circ_{1/2,3/2,5/2}$, denoted as $d_{5,6,7}$. Fine-structure splitting in the ground state of the recombined Ti^{3+} ion yields two $3p^63d(^2D_{3/2,5/2})$ levels, shown in Fig. 1 as b_1 and b_2, respectively. Radiative decay of all seven $3p^53d\{3d,4s\}$ near-threshold resonances is predominantly to the bound states due to the strong $\{3d,4s\}\to 3p$ core transitions.

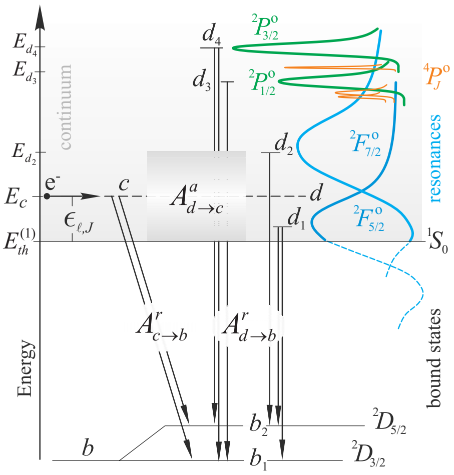

FIG. 1. (Color online) Schematic diagram of the most relevant near-threshold Ti^{4+} photorecombination pathways. Two broad, asymmetric $3p^53d^2(^2F^\circ_J)$ resonances straddle the first $3p^6(^1S_0)$ ionization limit $E^{(1)}_{th}=0$.

The partial cross section for PR of a free electron, at energy $\epsilon = E_c - E^{(1)}_{th}$ above the ground state $E^{(1)}_{th}$ of the target ion, into a bound state b of a recombined ion, is given by [46,63]

$$\sigma^{\mathrm{PR}}_{c\to b}(\epsilon) = \frac{8\pi}{3}\frac{g_b}{2g_{ion}}\frac{\alpha^3\omega^3_{c\to b}}{k\epsilon}|M_{b\to c}|^2, \tag{9}$$

where $\omega_{c\to b}$ is the frequency of the radiation field, k is the linear momentum of the continuum electron, g_b and g_{ion} are the statistical weights of the bound state b in the recombined ion and the ground state of the target ion, respectively. $M_{b\to c}$ is the complex photoionization (PI) matrix element of the corresponding transition and is expressed as

$$M_{b\to c} = \langle c|\mathbb{R}|b\rangle\left(1 + \sum_d \frac{Q^d_{b\to c} - \imath B^a_{d\to c}}{\varepsilon_d + \imath}\right). \tag{10}$$

The reduced c.m. energy, in the vicinity of a doubly excited state d, is given by the energy-detuning-from-resonance parameter $\varepsilon_d = 2(E_d - E_c)/\bar{\Gamma}_d$, with total width $\bar{\Gamma}_d = A^a_d + A^r_d$ and autoionization branching ratio $B^a_{d\to c} = A^a_{d\to c}/\bar{\Gamma}_d$. (The broad resonances d found in the near-threshold region have autoionization rates $A^a_{d\to c}$ much greater than radiative rates $A^r_{d\to b}$, and thus $B^a_{d\to c} \approx 1$.)

Note that, for a single resonance embedded in a single continuum and decaying to a single bound state, Eqs. (9) and (10) give a familiar Fano profile [64,65]. In particular, the partial PR cross section profile can be described as

$$\sigma = \sigma_a (q+\epsilon)^2/(1+\epsilon^2)$$

with an asymmetry parameter $q = Q^d_{b\to c}$ given by

$$Q^d_{b\to c} = \frac{\langle c|\mathbb{V}|d\rangle\langle d|\mathbb{R}|b\rangle}{(\bar{\Gamma}_d/2)\langle c|\mathbb{R}|b\rangle}. \tag{11}$$

In principle, the sum in Eq. (10) includes all $N^{J\pi}$-accessible doubly excited states d of a given symmetry $J\pi$. The total PR cross section is then obtained by summing Eq. (9) over all partial waves $J\pi$, all intermediate states d, and all recombined bound states b. To factor out the near threshold energy dependence, we consider an energy-scaled cross section

$$\epsilon\sigma^{\mathrm{PR}}(\epsilon) = \frac{8\pi}{3}\sum_{J\pi}\sum_{b=b_1}^{b_2}\frac{g_b}{2g_{ion}}\frac{\alpha^3\omega^3_{c\to b}}{k} \times |\langle c|\mathbb{R}|b\rangle|^2 \left|1+\sum_{d=1}^{N^{J\pi}}\frac{Q^d_{b\to c}-\imath}{\varepsilon_d+\imath}\right|^2. \tag{12}$$

D. Atomic structure and AUTOSTRUCTURE

Determination of partial and total perturbative (MCBP) DR cross sections requires the computation of autoionization and radiative rates of an exceedingly large number of resonances. To represent accurately the important Ti^{4+} $3p^6$ and $3p^5 3d$ N-electron target states, it is usually necessary to employ a configuration-interaction expansion including single-, double-, and even triple-electron promotions from the single-configuration description. We then construct all possible $(N+1)$-electron configurations by coupling a bound $(n\ell)$ or continuum $(\epsilon\ell)$ orbital to each N-electron configuration. For photoionized plasma temperatures $(k_B T \approx 1\ \mathrm{eV})$, core-excitation contributions from intrashell single-electron promotions $(\Delta n_c = 0)$ completely dominate over inter-shell excitations $(\Delta n_c \geqslant 1)$. This is also typical at collisionally ionized plasma temperatures $(4.7 < k_B T < 44.8\ \mathrm{eV}$ [66]) since our highest $3p^5 3d$ target level resides below the lowest $3p^5 4s$ level.

1. The Ti^{4+} target ion states

In order to compute accurately the atomic structure of an N-electron system, an optimal configuration interaction expansion is required. Of crucial importance is that the number of N-electron configurations used to describe all the target states should be small enough that the associated $(N+1)$-electron problem involving scattering, resonance, and recombined wave functions is computationally feasible. At this stage, we devote great care to determination of a bound orbital basis, $\{1s;2s;2p;3s;3p;3d;4s\}$, that has been optimized in the Slater-type-orbital model potential of Burgess, *et al.* [69] by varying the scaling parameters, $\lambda_{n\ell}$, to minimize the equally weighted-sum of MCBP eigenenergies of the nine lowest $3p^6$, $3p^5 3d$, and $3p^5 4s$ target terms, with mass-velocity and Darwin corrections included. The scaling parameters $\lambda_{n\ell}$ enter the potential by scaling the radial coordinate, as discussed by Eissner *et al.* [70] in the context of the Thomas-Fermi potential.

We then iteratively reoptimize the radial scaling parameters $\lambda_{3\ell}$ and λ_{4s} while "freezing" the closed-core parameters λ_{1s} and $\lambda_{2\ell}$. The purpose of such a reoptimization is not only to improve the initial energy levels in the Ti^{4+} ion, but, more importantly, to reproduce the critically evaluated data of Shirai *et al.* [68] for the dominant $3p^6(^1S_0) \to 3p^5 3d(^1P^\circ_1)$ radiative transition. The final stage of our successive reoptimization of radial functions is the confirmation of stationarity of the computed eigenenergies and radiative data with respect to small variations in λ_{nl} of both the core and valence orbitals. The resultant radial scaling parameters of the core orbitals are $\lambda_{1s} = 1.168\,38$, $\lambda_{2s} = 0.961\,23$, and $\lambda_{2p} = 1.008\,22$, whereas for the valence orbitals we obtain $\lambda_{3s} = 1.056\,53$, $\lambda_{3p} = 0.9895$, $\lambda_{3d} = 1.174$, and $\lambda_{4s} = 1.31$.

In Table I, we present MCBP eigenenergies as well as the best existing experimental data [68] for Ti^{3+} and Ti^{4+}. The differences between our results and the experimental values are less than 1%, except for the $3p^5 4s$ $(^3P^\circ_J)$ levels that are about 4% less than the NIST values [68]. This is an acceptable trade-off in the aforementioned optimization of one-electron orbitals, which prioritizes the radiative parameters in Table II for the dominant $3p^6(^1S_0) \to 3p^5 3d(^1P^\circ_1)$ core excitation. Thus it is customary to adjust empirically small deviations in computed energies for the target ion so that the series limits in the recombined ion match the excitation thresholds found in the NIST Atomic Spectra Database [71].

For resonant states converging to the $3p^5 3d$ $(^1P^\circ_1)$ limit, the dominant radiative decay pathways in Eq. (1) involve core relaxation of the inner $3d$ electron at a rate closely matching the dominant entry in Table II. The resonance strengths, as given in Eq. (4), intimately depend upon the accuracy of the most prevalent radiative rates.

Table II shows excellent agreement between calculated and observed radiative parameters for the strongest target-ion transitions—well within the experimental uncertainty of 18% [68]. Thus we are confident that the absolute strength of the computed DR cross section in the vicinity of the $3p^5 3d$ $(^1P^\circ_1)$ excitation threshold should be accurate to better than 18%.

2. The Ti^{3+} recombined ion

We have investigated all possible $(N+1)$-electron configurations that are constructed by attaching a bound, $n\ell$, or continuum, $\epsilon\ell$, orbital to the 17 target-ion thresholds listed in the upper part of Table I. The total DR cross section σ^{DR} is then routinely determined according to Eq. (3) by computing the relevant $(N+1)$-electron autoionization and radiative rates for all resonant states up to $n = 1000$ and $\ell = 0-10$.

An accurate atomic description of the near-threshold resonances is of particular importance, since this energy region is spanned by low-lying $3p^5 3d^2$ and $3p^5 3d 4\ell$ resonant features characterized by strong electron-electron correlation. The atomic structure calculations were performed using orbitals with radial scaling parameters $\lambda_{n\ell}$ optimized according to the following criteria. The energy of the ground state in the recombined Ti^{3+} ion together with its first ionization limit $E^{(1)}_{th}$ should closely match the values found in the NIST Atomic Spectra Database [71]. Therefore we report the converged scaling parameters for core orbitals to be $\lambda_{1s} = 1.168\,97$, $\lambda_{2s} = 0.996\,82$, and $\lambda_{2p} = 1.01$, followed by values for the valence

TABLE I. Energies (in Rydbergs and relative to the Ti^{4+} $3p^6(^1S_0)$ ground state) of the Ti^{4+} target states (top) and the Ti^{3+} initial bound and intermediate resonance states (bottom).

Ti^{4+}

K	Config.	Level	$K_{(\%)}$	Present[a]	MCHF[b]	NIST[c]
1	$3p^6$	$^1S_0$	$1_{(100)}$	0.00000	0.00000	0.00000
2	$3p^53d$	$^3P^\circ_0$	$2_{(99.9)}$	2.50011	2.36958	2.50088
3	$3p^53d$	$^3P^\circ_1$	$3_{(99.7)}$	2.50959	2.37796	2.50937
4	$3p^53d$	$^3P^\circ_2$	$4_{(99.1)}$	2.52884	2.39531	2.52704
5	$3p^53d$	$^3F^\circ_4$	$5_{(100)}$	2.61259	2.49031	2.61786
6	$3p^53d$	$^3F^\circ_3$	$6_{(98.1)}$	2.63191	2.50552	2.63402
7	$3p^53d$	$^3F^\circ_2$	$7_{(98)}$	2.65039	2.52032	2.64976
8	$3p^53d$	$^3D^\circ_3$	$8_{(75)}$; $12_{(25)}$	2.81151	2.67882	2.80150
9	$3p^53d$	$^1D^\circ_2$	$9_{(57)}$; $11_{(41)}$	2.82021	2.67384	2.79645
10	$3p^53d$	$^3D^\circ_1$	$10_{(99.7)}$	2.83290	2.69374	2.81811
11	$3p^53d$	$^3D^\circ_2$	$11_{(57.6)}$; $9_{(41.6)}$	2.83798	2.69581	2.81976
12	$3p^53d$	$^1F^\circ_3$	$12_{(73.9)}$; $8_{(24.2)}$	2.85083	2.71554	2.83799
13	$3p^53d$	$^1P^\circ_1$	$13_{(64.8)}$; $17_{(34.5)}$	3.62450	3.52383	3.60243
14	$3p^54s$	$^3P^\circ_2$	$14_{(99.9)}$	3.79145	3.82264	3.95799
15	$3p^54s$	$^3P^\circ_1$	$15_{(97.8)}$	3.82776	3.84568	3.98087
16	$3p^54s$	$^3P^\circ_0$	$16_{(99.9)}$	3.84828	3.87231	4.01017
17	$3p^54s$	$^1P^\circ_1$	$17_{(65.1)}$; $13_{(33.3)}$	4.00523	3.91017	4.04377

Ti^{3+}

K	Config.	Level lab.	$K_{(\%)}$	Theory		Experiment
1	$3p^63d$	$^3D_{3/2}$ b_1	$1_{(94)}$	−3.180079[a]		−3.180079[c] −3.180076[d,e] −3.180066[f,g]
2	$3p^63d$	$^3D_{5/2}$ b_2	$2_{(94)}$	−3.176457[a] −3.176279[h]		−3.176597[c] −3.176609[i,e]
58	$3p^53d^2$	$^2F^\circ_{5/2}$ d_1	$58_{(42.8)}$; $26_{(33.9)}$; $73_{(6.4)}$; $283_{(5.5)}$	0.009501[a] 0.009521[h]		0.014(6)[f,j,g] 0.02211[d,j,e]
59	$3p^53d^2$	$^2F^\circ_{7/2}$ d_2	$59_{(40.6)}$; $28_{(34.8)}$; $71_{(7.9)}$; $282_{(5.4)}$	0.026153[a] 0.023721[h]		0.02635[i,j,e] 0.033(3)[k,j,l]
62	$3p^53d4s$	$^2P^\circ_{1/2}$ d_3	$62_{(74.5)}$; $72_{(13.5)}$	0.084312[a] 0.066121[h]		0.084171[h,e]
64	$3p^53d4s$	$^2P^\circ_{3/2}$ d_4	$64_{(71.4)}$; $74_{(14.6)}$	0.100646[a] 0.081521[h]		0.101446[i,e] 0.099003[f,m,g]

[a] Present MCBP calculations (using 17 levels for Ti^{4+} and 360 levels for Ti^{3+}).

[b] MCHF (theoretical) [67].

[c] NIST (experimental) [68].

[d] VSS (experimental) [10].

[e] Vacuum spark spectroscopy.

[f] ALS (experimental) [12].

[g] PI of Ti^{3+}.

[h] CIV3 (theoretical) [14].

[i] VSS (experimental) [13].

[j] Unresolved $3p^53d^2(^2F^\circ)$.

[k] TSR (experimental) [24].

[l] PR of Ti^{4+}.

[m] Denoted as $3p^53d4s(^2F)$.

orbitals $\lambda_{3s}=1.112\,947$, $\lambda_{3p}=1.024\,559\,2$, $\lambda_{3d}=1.113\,85$, $\lambda_{4s}=1.1563$, $\lambda_{4p}=1$, $\lambda_{4d}=0.949$, and $\lambda_{4f}=1$.

The lower part of Table I illustrates the efficiency of this optimization by analyzing the resulting MCBP eigenenergies for certain low-lying bound and resonant states in the Ti^{3+} ion. Also shown for comparison are other recent theoretical and experimental results. Theoretically, Kingston and Hibbert [14] have performed bound-state calculations quite similar to our MCBP calculations (except here we are concerned with continuum states and higher-*n* states as well) using the well-established CIV3 code [72]. Multiconfiguration Hartree-Fock (MCHF) calculations have also been reported [67]. Experimentally, in addition to the Test Storage Ring (TSR) photorecombination (PR) measurements of Schippers, *et al.* [24], and the Advanced Light Source (ALS) photoionization (PI) measurements of Schippers, *et al.* [12], there

TABLE II. The breakdown of radiative data for transitions from the ground state of Ti^{4+} found in NIST database and obtained in this work. Numbers in square brackets are powers of 10.

Transition	A^r (ns^{-1})	S (a.u.)	f_ℓ	f_v
$3p^6(^1S_0)\rightarrow 3p^5 3d(^1P^\circ_1)$	1.283[+2]	3.018	3.65	3.16
	1.263[+2]$^{\mathrm{a,b}}$	3.02$^{\mathrm{a,b}}$	3.63$^{\mathrm{a,b}}$	
$3p^6(^1S_0)\rightarrow 3p^5 3d(^3D^\circ_1)$	5.8[−2]	2.87[−3]	2.7[−3]	3.3[−3]
	4.0[−2]$^{\mathrm{a,c}}$	2.0[−3]$^{\mathrm{a,c}}$	1.9[−3]$^{\mathrm{a,c}}$	

[a] NIST [68].
[b] Assigned experimental uncertainties: $\lesssim 18\%$.
[c] Assigned experimental uncertainties: $\gtrsim 50\%$.

exist the vacuum spark spectroscopy (VSS) observations of Ryabtsev *et al.* [13] and the NIST values [68].

If the inverse reaction in Eq. (1) is of main interest, then, using the principle of detailed balance, as discussed further below, we can study Ti^{3+} PI cross sections from each bound state to the pertinent electron continua. For this purpose, Table III lists our calculated parameters for radiative transitions between ground and near-threshold configurations in Ti^{3+}.

We can see from Table III that our MCBP rates are systematically higher than other existing data [13,14]. Nevertheless, for the dominant radiative transitions, our results are within 5% of the experimental values whereas the CIV3 rates are about 28% lower, despite their resonance positions coinciding well with ours (see Table I).

III. REDUCTION OF PR DATA

The superior quality of DR data obtained using merged ion and electron beams is unquestionably the main reason why investigations of this fundamental recombination process are now performed almost exclusively at ion storage ring facilities equipped with electron coolers. The latest generation of heavy-ion storage ring facilities [73] allows direct measurement (in absolute scale) of the PR rate coefficient with an unprecedented energy resolution. This in turn offers a fruitful test ground for sophisticated computational techniques, such as relativistic many-body perturbation theory and its estimates of the screened quantum electrodynamical effects in lithiumlike ions [74].

The only experimental work on PR of Ti^{4+} ions was performed at TSR Heidelberg [24] in which an overall velocity-averaged rate coefficient was reported. In this section we offer a brief overview of all necessary steps that were undertaken in our theoretical interpretation of these experimental findings.

TABLE III. Comparison of computed radiative decay data for selected near-threshold resonances in Ti^{3+} that are relevant to the investigation of interference effects.

Transition	Label	A^r (ns^{-1})	S (a.u.)	f
$3p^6 3d(^2D_{3/2})\rightarrow 3p^5 3d^2(^2F^\circ_{5/2})$	$b_1\rightarrow d_1$	97.1	6.707	1.783
		92.5$^{\mathrm{a}}$		
		66.1$^{\mathrm{b}}$		1.213$^{\mathrm{b}}$
$3p^6 3d(^2D_{5/2})\rightarrow 3p^5 3d^2(^2F^\circ_{5/2})$	$b_2\rightarrow d_1$	5.52	0.382	0.067
		3.99$^{\mathrm{b}}$		0.049$^{\mathrm{b}}$
$3p^6 3d(^2D_{5/2})\rightarrow 3p^5 3d^2(^2F^\circ_{7/2})$	$b_2\rightarrow d_2$	103.4	9.403	1.673
		99.5$^{\mathrm{a}}$		
		71.2$^{\mathrm{b}}$		1.155$^{\mathrm{b}}$
$3p^6 3d(^2D_{3/2})\rightarrow 3p^5 3d4s(^2P^\circ_{1/2})$	$b_1\rightarrow d_3$	19.3	0.403	0.111
		19.4$^{\mathrm{a}}$		
		17.6$^{\mathrm{b}}$		0.104$^{\mathrm{b}}$
$3p^6 3d(^2D_{3/2})\rightarrow 3p^5 3d4s(^2P^\circ_{3/2})$	$b_1\rightarrow d_4$	2.3	0.093	0.026
		2.1$^{\mathrm{b}}$		0.024$^{\mathrm{b}}$
$3p^6 3d(^2D_{5/2})\rightarrow 3p^5 3d4s(^2P^\circ_{3/2})$	$b_2\rightarrow d_4$	18.1	0.74	0.137
		16.2$^{\mathrm{b}}$		0.127$^{\mathrm{b}}$

[a] Experimental (VSS) [13].
[b] Theoretical (CIV3) [14].

A. Theoretical PR rate coefficient

The standard approach [75] for comparing theoretical calculations to experimental measurements is to compute the PR cross section σ^{PR} and convolute it with the anisotropic Maxwellian distribution of electron velocities [76]:

$$\alpha_{\mathrm{theor}}(\Delta v) = \int d^3\vec{v}\, v\, \sigma^{\mathrm{PR}}(v) f(\vec{v},\Delta v). \tag{13}$$

Here $f(\vec{v},\Delta v)$ is a strongly anisotropic distribution function involving the transverse and longitudinal velocity components, $v_\perp$ and $v_\parallel$, of the incident electron. These are parametrized in turn by the corresponding temperatures, $k_{\mathrm{B}}T_\perp$ and $k_{\mathrm{B}}T_\parallel$, that dictate the shape of the DR resonances. Δv is the detuning of the electron longitudinal velocity in the c.m. frame of the ions.

This particular form of presenting the PR data is problematic at low energies in that the shape of DR resonances is strongly affected by the electron beam transverse temperature, $k_{\mathrm{B}}T_\perp$. Namely, besides an energy dependent broadening, the convolution in Eq. (13) introduces an additional redshift and asymmetry of resonances. For example, using the TSR experimental parameters reported by Schippers *et al.* [24], any narrow resonance found within $\epsilon = k_{\mathrm{B}}T_\perp$ will, after convolution, possess a full width at half maximum (FWHM) of $\Delta\epsilon_{1/2} \approx 1.1 \times k_{\mathrm{B}}T_\perp$ and will be shifted to lower energies by $\delta\epsilon_- \approx 0.25 \times k_{\mathrm{B}}T_\perp$. Furthermore, in this example the convolution in Eq. (13) introduces $\approx 17\%$ of the red asymmetry in the resulting rate coefficient profile. Given the additional asymmetry, shift, and width introduced by the cooler distribution, it would seem desirable to filter out these effects. Thus any accurate assessment of resonance positions, widths, and shapes would benefit by direct comparison between the theoretical prediction for σ^{PR} and an experimental "cross section," which in turn can be obtained, in principle, by deconvoluting the measured rate coefficient using Eq. (13).

B. Deconvolution of experimental PR spectra

We have developed a deconvolution procedure that is able to convert the measured PR rate coefficient α_{expt} and produce a cross section $\sigma^{\mathrm{PR}}_{\mathrm{expt}}$ for the broader features of the recombi-

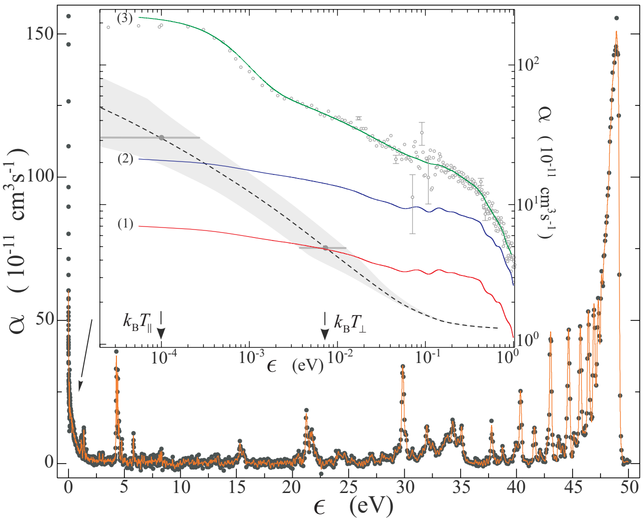

FIG. 2. (Color online) The lower portion of the figure illustrates the outcome of a fully converged, hundred-iteration deconvoluted cross section that is then reconvoluted (red solid curve) to closely follow the experimental rate coefficient (circles). The inset shows different stages in the deconvolution of the low-energy part of the experimental data: (1) red curve, initial estimate; (2) blue curve, fifth iteration; (3) green curve, slowly converged 500-iteration results. The shaded pattern represents an energy dependent FWHM of the rate coefficient spectra for experimental temperatures $k_BT_\parallel = 0.1$ meV and $k_BT_\perp = 7.3$ meV.

nation spectrum. Here we outline only the main deconvolution features; further details are given in [77]. First, integration over the velocity space in Eq. (17) is performed in the c.m. energy domain. In this setting, the angular integration is carried out by use of the Gauss-Kronrod quadrature formula [78,79], while integration over c.m. energies follows the adaptive algorithm given in [77]. Second, besides the experimental rate coefficient α_{expt}, the only required input is the electron beam transverse $k_BT_\perp$ and longitudinal $k_BT_\parallel$ temperatures, which must be deduced from the experimental conditions [24].

We begin our iterative deconvolution by guessing the initial estimate for the underlying experimental cross section $\sigma_{\text{expt}}^{\text{PR},(0)}$. One frequently used estimate assumes monoenergetic electrons (an "apparent" cross section) [80], and is obtained by dividing the rate coefficient by the velocity: $\sigma_{\text{expt}}^{\text{PR},(0)} = \alpha_{\text{expt}}/v$. We note that another choice may simply be an arbitrary number without significant computational penalty. By convoluting through Eq. (13), we arrive at a first approximation $\alpha_{\text{expt}}^{(1)}$ for the experimental rate coefficient, which corresponds to the red colored curve$^{(1)}$ found in the inset of Fig. 2. In the next step, we deconvolve the residual $\alpha_{\text{expt}}^{(1)} - \alpha_{\text{expt}}$ with help of the set of Λ_k functions [77] evaluated at Gauss-Kronrod abscissas ω_k. This step gives us the correction $\Delta\sigma$ that is then added to the initial guess $\sigma_{\text{expt}}^{\text{PR},(0)}$, resulting in an updated guess for the cross section $\sigma_{\text{expt}}^{\text{PR},(1)}$. The convolution of such an updated cross section constitutes the second iteration and leads to an improved approximation $\alpha_{\text{expt}}^{(2)}$ for the experimental rate coefficient. We then repeat this process until the successive corrections become sufficiently small, giving us the converged synthetic PR cross section $\sigma_{\text{expt}}^{\text{PR}}$ that will reproduce the experimental rate coefficient when used in Eq. (13).

Convergence of this algorithm depends on the signal-to-noise ratio of the experimental data. Any strong scattering of experimental points within a FWHM of the distribution function, $f(\vec{v},\Delta v)$, will be propagated through the deconvoluted cross section due to the inability of $f(\vec{v},\Delta v)$ to follow "unexpected" changes. Noise propagation induces a slow adjustment of the deconvoluted cross section points, spreads itself in energy region around strong irregularities, and requires a larger number of iterations until convergence is met. This conclusion is supported by Fig. 2, where, at energies above 1 eV, full convergence is achieved after 100 iterations. However, as the inset of Fig. 2 shows, for energies below 1 eV, the rate of convergence is five times slower, for two reasons. First, for a collision energy of $\epsilon = k_BT_\parallel$, the rate coefficient $\alpha_{\text{theor}}(\epsilon)$ has FWHM of about $2.2k_BT_\parallel$ that is too broad to account efficiently for its sudden increase at $\epsilon \approx 1$ meV. Namely, even for bare ions, the measured recombination rates at very low energies show strong enhancements over the standard predictions [81]. This enhancement is understood to arise primarily from transient field-induced recombination during the merging process of electron and ion beams [82] and its modeling is beyond the scope of this work as it requires a detailed knowledge of the experimental setup. Second, for collision energies below 185 meV, the experimental spectra contain a noisy pattern in the vicinity of the d_1 resonance, and it is here that convergence is slowest. It is worth noticing that the experimental rate coefficient of isoelectronic Sc^{3+} ions [48] also suffers from a similar noisy pattern at about 3 eV. The origin of this oscillatory feature in the experimental data is unclear since our MCBP results, and those of Ref. [14], support the conclusion that below ≈ 0.4 eV there are only broad $d_{1,2}$ resonances.

C. Maxwellian-averaged PR rate coefficients

In the case of an isotropic Maxwellian plasma with temperature T, the incoherent DR (Lorentzian) contributions in Eq. (13) yield a smooth and broad Maxwellian rate coefficient that possesses distinct maxima at certain temperatures $2/3E_i$, and may be modeled accurately by the fitting formula

$$\alpha^{\text{DR}}(T) = T^{-3/2} \sum_i c_i \exp(-E_i/T). \tag{14}$$

In the case of plasmas that are not in local thermodynamic equilibrium, a parametrized entropic form of $\alpha^{\text{DR}}(T)$ may be used instead [83]. Over a wide range of temperatures present in stellar atmospheres, any underlying resonant structure in the computed DR cross section becomes smeared out. However, in certain environments like H II and starburst regions [84], where the photoionized plasma temperature T is less than ≈ 1 eV, the low-energy resonant features play a decisive role in the nature of the emitted radiation.

To illustrate this further, we show the present MCBP results for the Ti^{4+} Maxwellian rate coefficients in Fig. 3, and we make a number of comparisons in Table IV. First, as Fig. 3 reveals, at low plasma temperatures ($k_BT < 1$ eV) the total DR contribution is an order of magnitude larger than the RR.

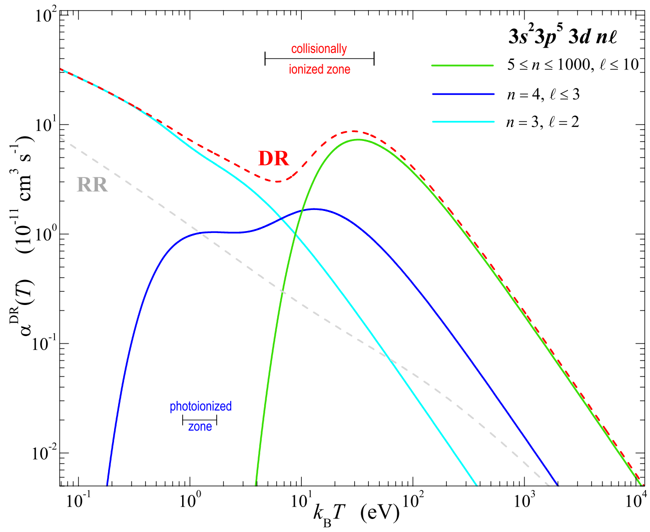

FIG. 3. (Color online) Field-free Maxwellian rate coefficients for Ti^{4+}; see Table IV. Red dashed curve, total DR due to $3p^53dn\ell$ resonances; grey dashed curve, total RR with $\ell_{max}=200$.

This is due to the strong, near-threshold $3p^53d^2$ and $3p^53d4\ell$ resonances. Second, Fig. 4 addresses the discrepancy of 45% and 144% among the current high-temperature DR results and those of Hahn [85] and Landini *et al.* [86], respectively. We note that the empirical rate formula of Hahn [85] incorporated fitting parameters via the modified atomic transport code MIST [87]. Intriguingly, the previously recommended DR data of Mazzotta, *et al.* [88] agree within 6% of our $n \geqslant 5$ DR contribution, even though their compilation refers to the empirical results of Hahn [89]. Namely, DR data of Mazzotta *et al.* [88] are inferred by using the Burgess general formula [90]. However, these data are then scaled down by the same factor of 0.426 that had been used to align the Burgess results for Fe^{8+} with the results of Hahn [89]. In their study, Mewe *et al.* [91] used the parametrized empirical formula based upon the renormalized results of Jacobs *et al.* [92] and Ansari *et al.* [93] for $3p \rightarrow 3d$, $3p \rightarrow 4s$, and $3p \rightarrow 4d$ core excitations in Fe^{8+}. However, the discrepancy of 163% between our present results and those of Mewe *et al.* [91] cannot be attributed to our under-representation of all possible $3p \rightarrow 4\ell$ core excitations since our preliminary calculations show that these resonances contribute $\lesssim 5\%$ to the high-temperature peak in Fig. 4. Our present RR contribution is computed over the temperature range 1.6×10^2–1.6×10^8 K following the methodology of Badnell [94] and shown in Fig. 3. It is twice the recommended value of Mazzotta *et al.* [88], and may be reproduced with ±1% accuracy by using the functional form [94–96],

$$\alpha^{RR}(T) = \frac{A\sqrt{T_0/T}}{(1+\sqrt{T/T_0})^{p_-}(1+\sqrt{T/T_1})^{p_+}},$$

with the following fitting parameters: $A=3.989\times10^{-10}$ cm^3 s^{-1}, $B=0.5658$, $C=0.1065$, $T_0=95.17$ K, $T_1=4.776\times10^{+7}$ K, $T_2=3.534\times10^{+5}$ K, and $p_\pm = 1 \pm B \pm C\exp(-T_2/T)$.

TABLE IV. Fitting coefficients E_i (K) and c_i (cm^3 s^{-1} K$^{3/2}$) for the Ti^{4+} ground state DR rate coefficient as given by Eq. (14). Uncertainties are determined as the maximum deviation between fitted and computed rate coefficients over the temperature range 1.6×10^2–1.6×10^8 K and are enclosed in parentheses, where $v^{[\pm p]}_{(u)}$ denotes $v(u)\times10^{\pm p}$.

E_1	E_2	E_3	E_4	
c_1	c_2	c_3	c_4	Config.
$4.098^{[+5]}_{(3)}$	$5.646^{[+5]}_{(2)}$			
$1.880^{[-3]}_{(2)}$	$7.264^{[-2]}_{(3)}$			$3s^23p^53dn\ell$[a]
$2.062^{[+4]}_{(5)}$	$1.026^{[+5]}_{(9)}$	$3.003^{[+5]}_{(3)}$		
$7.225^{[-5]}_{(4)}$	$5.251^{[-4]}_{(4)}$	$4.891^{[-3]}_{(1)}$		$3s^23p^53d4\ell$[b]
$1.183^{[+1]}_{(6)}$	$6.846^{[+1]}_{(4)}$	$2.055^{[+2]}_{(2)}$	$5.352^{[+2]}_{(4)}$	
$2.730^{[-7]}_{(2)}$	$7.707^{[-7]}_{(7)}$	$1.813^{[-6]}_{(3)}$	$4.580^{[-6]}_{(5)}$	$3s^23p^53d^2$
E_5	E_6	E_7	E_8	
c_5	c_6	c_7	c_8	Config.
$1.395^{[+3]}_{(5)}$	$3.728^{[+3]}_{(2)}$	$1.015^{[+4]}_{(3)}$	$4.651^{[+4]}_{(7)}$	
$1.265^{[-5]}_{(2)}$	$3.535^{[-5]}_{(2)}$	$6.775^{[-5]}_{(5)}$	$3.338^{[-4]}_{(7)}$	$3s^23p^53d^2$

[a] $5 \leqslant n \leqslant 1000$, $\ell \leqslant 10$.
[b] $\ell \leqslant 3$.

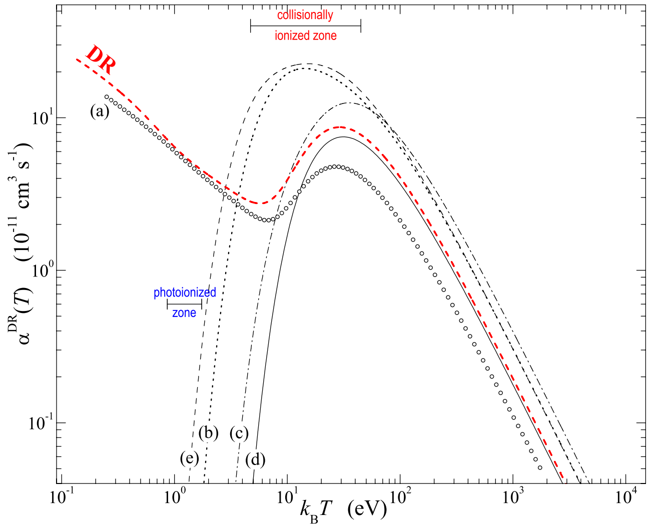

FIG. 4. (Color online) Comparison of existing field-free Maxwellian-averaged DR ground-level rate coefficients for Ti^{4+}. Red dashed curve, total DR due to $3p^53dn\ell$ resonances; (a) black open circles, field-influenced TSR experiment by Schippers *et al.* [24]; (b) black dotted curve, compilation by Landini and Monsignori [86]; (c) black dash-dotted curve, empirical formula of Hahn [85]; (d) black solid curve, recommended value by Mazzotta *et al.* [88]; (e) black dashed curve, empirical results of Mewe *et al.* [91]. A typical electron-collisional [66] and photoionized [97] plasma temperature ranges for Ti^{4+} are also indicated.

IV. RESULTS AND ANALYSIS

We now outline the relevant theoretical aspects, including the important low-n interference effects (in both PR and PI) and the high-n external electric field effects, that need to be included in our calculations. Results are then shown in vari-

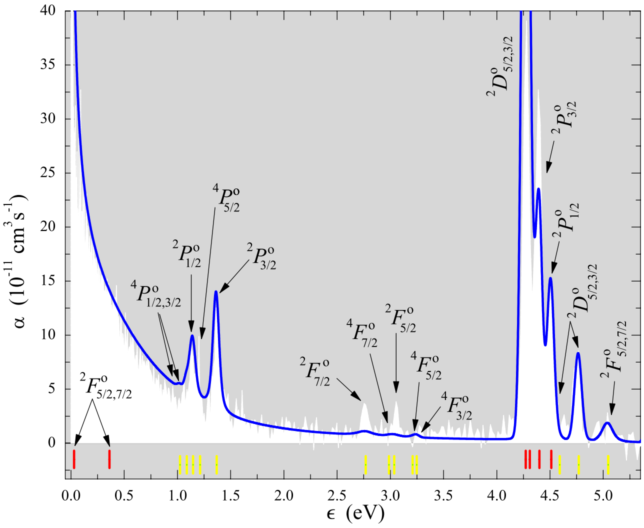

FIG. 5. (Color online) Overview of Ti^{4+} rate coefficient spectra for low collisional c.m. energies. The color code used for these field-free calculations are as follows: red bars, position indicators for $3p^53d^2$ resonances; yellow bars, position indicators for $3p^53d4s$ resonances; blue curve, total DR rate coefficient obtained in the present work; white area, TSR experiment [24].

ous energy regions and compared to the experimental Ti^{4+} PR spectrum [24] and the Ti^{3+} PI spectrum [12].

A. Low-energy region

Figure 5 enlarges a part of the experimental spectra in the energy range 0–5.5 eV. Interpretation of experimental features relies on current field-free computations of resonance positions, strengths, and widths, as discussed in Sec. II D. We begin with a detailed analysis of the resonance features seen in Fig. 5, where all parameters given are from our MCBP calculations, except where noted.

The spectrum below 1 eV is dominated by two broad $3p^53d^2(^2F^\circ_{5/2,7/2})$ resonances, with convoluted contributions at resonance that are about ten times the background RR contribution (see Fig. 3). A group of five $3p^53d4s$ resonances is also determined to exist between 1 and 1.5 eV, but only the two $^2P^\circ_{1/2,3/2}$ states are strong enough to be seen on this scale. It is interesting to note, in Figs. 5 and 7, that the experimental rate coefficient exhibits a narrow peak at 1.213 eV, precisely where our calculations predict the existence of a weak $3p^53d4s(^4P^\circ_{5/2})$ resonance.

A further analysis of this near-threshold region below ≈1.5 eV is given in Sec. IV A 1 since there we need to consider interference effects. We proceed with our lowest-order MCBP description of the two $3p^53d4s(^2F^\circ_{7/2,5/2})$ resonances located at 2.768 and 3.037 eV. These positions are in good agreement with the experimental VSS values of 2.772 and 3.063 eV, but about 0.4 eV lower than the theoretical CIV3 positions [14]. For the $3p^53d4s(^2F^\circ_{7/2})$ resonance, our total width $\bar{\Gamma}_d = 151$ meV is essentially due to autoionization $A^a_{d\to c} \gg A^r_{d\to b}$, and the integrated strength $\mathcal{S}^d$ as given in Eq. (4) is therefore dependant only on the dominant radiative rate $A^r_{d\to b_2} = 1.5\ \mathrm{ns}^{-1}$. This is about six times smaller than the experimental TSR value inferred from the peak height in Fig. 5, and about 2.7 times smaller than the experimental VSS value. A similar conclusion is reached for the nearby $3p^53d4s(^2F^\circ_{5/2})$ resonance, having a total width of 90 meV. These resonances are members of a weak Rydberg series converging to the $3p^53d(^3F^\circ_J)$ limits, as illustrated in Fig. 9, and failure to reproduce accurately the resonance strengths is the consequence of a trade-off introduced during orbital optimization on the dominant ionic core excitation $3p^6(^1S_0) \to 3p^53d(^1P^\circ_1)$, as discussed in Sec. II D.

The most prominent features seen in Fig. 5 are the two $3p^53d^2(^2D^\circ_{5/2,3/2})$ resonances at 4.272 and 4.310 eV, respectively; these are within 225 meV of the experimental VSS value [13]. The total integrated strength of the $3p^53d^2(^2D^\circ_{5/2})$ resonance obtained in this work is $\mathcal{S}^d \approx 2.1\ \mathrm{Mb\,eV}^2$ and predominantly comes from radiative decay into the state b_2. This is because the autoionization in Eq. (4) dominates ($A^a = 1367.5\ \mathrm{ns}^{-1} \gg A^r = 149.6\ \mathrm{ns}^{-1}$), and thus $\mathcal{S}^d \propto A^r$. The experimental VSS value of $A^r = 163.6\ \mathrm{ns}^{-1}$ [13] is 9% higher and cannot be entirely due to the difference in transition energies.

The $3p^53d^2(^2D^\circ_{3/2})$ resonance, on the other hand, has an autoionization rate of $A^a = 101.5\ \mathrm{ns}^{-1}$, which is comparable to its radiative decay rate $A^r = 119.8\ \mathrm{ns}^{-1}$ into the ground state, and it is in good agreement with the experimental VSS value $A^r = 128.5\ \mathrm{ns}^{-1}$ [13]. Thus its overall integrated strength is $\mathcal{S}^d \approx 0.6\ \mathrm{Mb\,eV}^2$. This is an example of how strong an influence the branching ratio for radiative decay in Eq. (4) may have on the DR resonance strengths; even though the dominant radiative transition rates are within 10% of the experimental VSS values [13], the total experimental TSR strength of the $^2D^\circ$ composite peak in Fig. 5 appears to be 2.3 times weaker than the calculated strength.

For the $3p^53d^2(^2P^\circ_{3/2})$ resonance at 4.401 eV, our computed total integrated strength of $\mathcal{S}^d \approx 0.66\ \mathrm{Mb\,eV}^2$ is about 30% lower than the experimental TSR value. However, its position agrees well with the experimental VSS value of 4.391 eV [13]. This resonance radiatively decays into b_1 and b_2 bound states with rates of 21.1 and 51.4 ns^{-1}, respectively, and autoionizes at a rate of 774.5 ns^{-1}, implying that the integrated strength depends mostly on the radiative decay rates that are, in this case, about half the VSS value. Furthermore, our autoionization width of 0.5 meV is much smaller than the VSS value of 9.9 meV.

The last resonance from $3p^53d^2$ configuration is identified in Fig. 5 as $^2P^\circ_{1/2}$ with position 4.512 eV, total width 1.2 meV, and integrated strength 0.446 $\mathrm{Mb\,eV}^2$ matching the TSR experiment very well. However, the VSS experimental position is somewhat lower at 4.266 eV, the VSS radiative rate into b_1 is 51% larger (143 ns^{-1}), and the VSS autoionizing width of 16.1 meV exceeds our computed value of 1.17 meV. At 4.591 eV, the $3p^53d4s(^2D^\circ_{5/2})$ resonance is too weak to be of any significance to the present analysis. The stronger $3p^53d4s(^2D^\circ_{3/2})$ resonance parameters show good agreement between the theoretical and TSR experimental values; both agree in position (≈4.77 eV), total width (≈0.7 meV), and integrated strength (≈0.25 $\mathrm{Mb\,eV}^2$). The dominant radiative rates are 15.3 and 10.8 ns^{-1} into b_1 and b_2 bound states, respectively, and the autoionization rate is $A^a = 1060.7\ \mathrm{ns}^{-1}$.

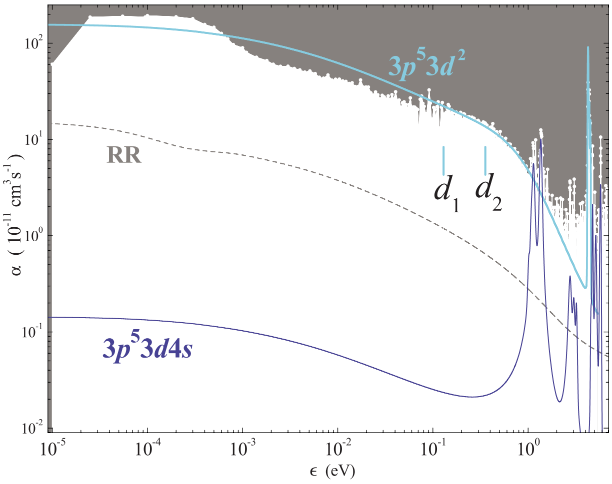

FIG. 6. (Color online) Dominant part of the Ti^{4+} rate coefficient spectra consisting of near-threshold states: white area, TSR experiment [24]; solid curves, contributions coming from $3p^53d^2$ (cyan) and $3p^53d4s$ (blue) resonances; grey dotted curve, nonresonant RR contribution.

We conclude our analysis of the low energy region with the $3p^53d4s(^2F^\circ_{5/2,7/2})$ resonances at 5.046 eV. Both resonances have comparable autoionization rates, 0.11 and 0.13 fs^{-1}, but most of the integrated strength ($\mathcal{S}^d = 0.11$ Mb eV^2) derives from radiative decay of the $^2F^\circ_{5/2}$ resonance into the bound state b_2 at a rate of $A^r = 7.3$ ns^{-1}. The $^2F^\circ_{5/2}$ experimental VSS resonance is reported at 5.0 eV, well separated from the $^2F^\circ_{7/2}$ resonance at 5.1 eV, and has an autoionization width that is 0.8 times our MCBP value and a radiative width that is 2.8 times our MCBP value.

1. Near-threshold photorecombination

We now investigate the lowest $3p^6$ threshold region ($\epsilon \to 0$, see Fig. 6), where we are primarily interested in comparisons between detailed theoretical and experimental resonance profiles in order to quantify further resonance interference effects. We evaluated our higher-order PR expression in Eq. (12) using the computed resonance parameters shown in Table V for the most important near-threshold resonances. Since the PR cross section $\sigma^{PR}(\epsilon)$ has a $1/\epsilon$ type dependence, we focus instead on the scaled quantity $\epsilon\sigma^{PR}(\epsilon)$, see Eq. (12), in order to factor out the threshold divergence.

A comparison between lowest-order and higher-order theoretical results and experimentally inferred results for the scaled PR cross section are given in Fig. 7. Strong resonance-background interference effects are clearly seen. Inclusion of the (finite) asymmetry parameters from Table V leads to asymmetric $^2F^\circ$ resonances as opposed to the IP-IRDW symmetric Lorentzian profiles.

We note that Eq. (12) could be used as a fitting function with optimized resonance profile parameters to reproduce the deconvoluted TSR experimental results [24]. However, we choose instead to use our same computed atomic data for the purpose of comparison with high-resolution synchrotron facility photoionization measurements [12]. As is demonstrated, there is a much better level of agreement between computed and measured resonance profiles, indicating an inconsistency between the theoretically deconvoluted experimental PR spectra and the direct PI measurements.

TABLE V. The comparison of partial autoionization rates $A^a_{d\to c}$ and asymmetry parameters $Q^d_{c\to b}$ for selected near-threshold resonances formed in Ti^{3+} that are relevant for investigation of interference effects. Numbers in brackets are experimental uncertainties, where available.

Transition	Label	$A^a_{d\to c}$ (fs^{-1})	Label	$Q^d_{c\to b}$
$3p^53d^2(^2F^\circ_{5/2})$	$d_1\to c$	2.55^a	$\overset{d_1}{c\to b_1}$	6.16^a
$\searrow 3p^6\epsilon f(^2F^\circ_{5/2})$		2.19^b $1.42(6)^c$	$\overset{d_1}{c\to b_2}$	-5.51^a
$3p^53d^2(^2F^\circ_{7/2})$	$d_2\to c$	2.54^a		
$\searrow 3p^6\epsilon f(^2F^\circ_{7/2})$		$2.28(15)^{d,e}$ $1.82(18)^{e,f}$	$\overset{d_2}{c\to b_2}$	6.16^a
$3p^53d4s(^2P^\circ_{1/2})$	$d_3\to c$	0.056^a	$\overset{d_3}{c\to b_1}$	232^a
$\searrow 3p^6\epsilon p(^2P^\circ_{1/2})$		$0.060(3)^c$		
$3p^53d4s(^2P^\circ_{3/2})$	$d_4\to c$	0.052^a	$\overset{d_4}{c\to b_1}$	261^a
$\searrow 3p^6\epsilon p(^2P^\circ_{3/2})$		$0.079(3)^c$	$\overset{d_4}{c\to b_2}$	247^a

[a] Present MCBP calculations using a 360-level nonorthogonal basis expansion from Ti^{3+} ground state.
[b] VSS experiment [10].
[c] VSS experiment (Table 1 of Ref. [13]).
[d] ALS PI experiment [12].
[e] Fit of unresolved experimental resonances.
[f] TSR PR experiment [24].

2. Near-threshold photoionization

Using Eqs. (9)–(12), and the principle of detailed balance,

$$\sigma^{PI}_{b\to c} = \frac{2g_{ion}}{g_b\alpha^2\omega^2_{b\to c}}\epsilon\sigma^{PR}_{c\to b}, \tag{15}$$

photoionization results are easily and accurately computed. This is helpful for studying further the near threshold resonance region because recent synchrotron radiation measurements have also been performed for Ti^{3+} [12].

The comparison of Fig. 8 leads to the conclusion that the degree of interference effects in the theoretical PI spectrum of Ti^{3+} have been indirectly confirmed experimentally through ALS studies.

The inset in Fig. 8 reveals the details about the underlying photoabsorption transitions in the composite PI pattern. Contrary to the fractional metastable abundance inferred from ALS studies [12], we use the statistical values of $3p^63d(^2D_{3/2})$ and metastable $3p^63d(^2D_{5/2})$ abundances of $\eta_{3/2}=4/10$ and $\eta_{5/2}=6/10$. The experimental values reported were instead $\eta_{3/2}=0.45(2)$ and $\eta_{5/2}=0.55(2)$ [12]. In addition, to account for the finite experimental photon energy resolution, the theoretical cross sections shown in Fig. 8 were convoluted with energy-dependent FWHM Gaussians spanning ≈20–80 eV [12].

As a further investigation into these strong asymmetry effects, we performed independent, nonperturbative calcula-

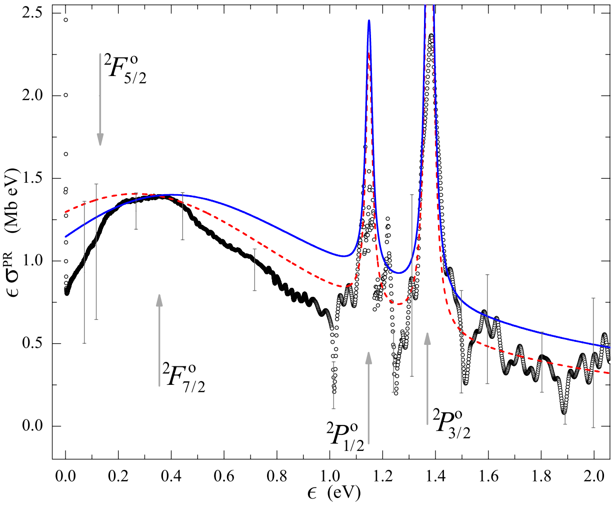

FIG. 7. (Color online) Demonstration of interference effects found in the near-threshold region of PR spectra of Ti^{4+}: black points, deconvoluted TSR of Schippers *et al.* [24]; red dashed curve, lowest-order perturbation method result of Eq. (3), and blue solid curve as its next-highest order modification in the form of Eq. (12) containing interference effects.

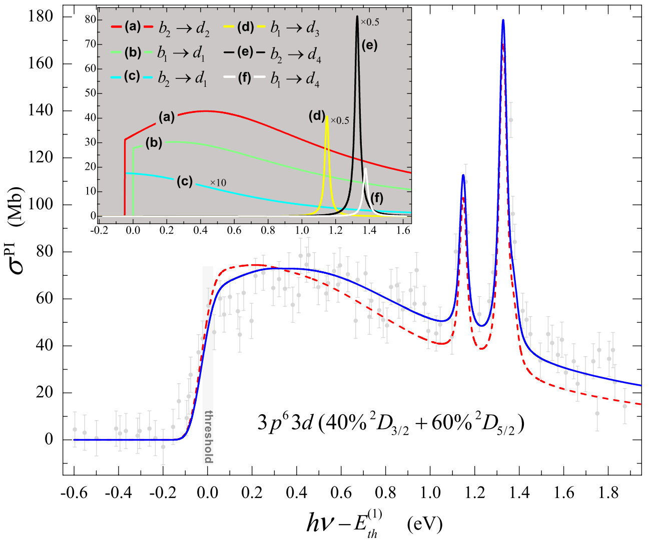

FIG. 8. (Color online) Comparison between computed and experimental PI cross sections for Ti^{3+}. Gray points with error bars, merged photon-ion beams experiment of Schippers *et al.* [12]; theoretical PI cross sections computed via Eq. (15): red dashed curve, IPIRDW using Eq. (3); blue solid curve, using Eq. (12) including interference effects. The inset identifies the structure of the composite blue solid curve, where the heights of certain resonances have been modified only to conform visually to the rest of the curves. The energy scale is given relative to the first ionization threshold $E^{(1)}_{th}$=43.267 eV.

tions using the well-established R-matrix method [98,99] that incorporates interference effects and has been improved upon by including various types of radiation damping [100–102]. This approach was used together with our present higher-order perturbative method to predict the strong asymmetry in the $3p^5 3d^2$ resonances in photorecombination of Sc^{3+} [46]. However, as in that study, convergence of atomic structure in the present study, most notably the near-threshold resonance positions, was not achieved due to the orthogonal-basis restriction of this particular R-matrix implementation. Nevertheless, our resultant PR or PI resonance profiles, while having resonance positions well above threshold (≈1.0–1.2 eV), and therefore contributing fully to the cross section, still exhibited the same overall good asymmetry agreement with the experimental and/or theoretical results shown in Fig. 8. While we could proceed to increase the orbital and/or configuration basis so as to bring our orthogonal-basis atomic structure calculations to convergence, we have learned that recent R-matrix calculations for photoionization of Sc^{2+} and Ti^{3+} [103,104] are well underway toward achieving convergence.

B. Intermediate-energy region

Interpretation of the complex experimental TSR spectra above 5.5 eV requires consideration of multiple, overlapping Rydberg series of resonances, as illustrated in Fig. 9. For brevity, we focus on the most prominent and unambiguous resonant features. The four $3p^5 3d4s(^2D^\circ_{3/2,5/2})$ and $3p^5 3d4s(^2P^\circ_{3/2,1/2})$ resonances give two prominent peaks at 5.8 and 15.4 eV, respectively. The strongest is the $3p^5 3d^2(^2P^\circ_{3/2})$ resonance at 15.379 eV, with total integrated strength of $\mathcal{S}^d$=1.71 Mb eV^2 and total width of 146 meV. In between are 60 $3p^5 3d4p$ states, and the $3p^5 3d4d$ members with the strongest $^2D^\circ_{5/2,3/2}$ resonances at 20.507 eV.

Five additional $3p^5 3d4p$ resonances are found at around the 20 eV region: $^2P_{1/2,3/2}$ at 21.23 eV, $^2D_{3/2,5/2}$ at 21.65 eV, and $^2S_{1/2}$ at 22.09 eV.

The triple-peak structure at 24.3 eV and the peak at 35.08 eV are due to the $3p^5 3d4f$ resonances, and the strongest radiative decay of the two $^2G_{7/2,9/2}$ resonances at 35.08 eV states is to the $3p^6 4f(^2F^\circ_{5/2,7/2})$ bound states at rates of 110.8 and 121.1 ns^{-1}, respectively. In between are three composite peaks of $3p^5 3d4d$ resonances: $^2F^\circ_{5/2,7/2}$ at 29.8 eV, $^2P^\circ_{1/2,3/2}$ at 31.9 eV, and $^2D^\circ_{5/2,3/2}$ at 33.7 eV. It is in this region that different Rydberg series start to overlap. For example, nine $3p^5 3d(^1P^\circ_1)n\ell$ resonances with n=5 overlap with three relatively strong peaks at 32.3 and 37.8 eV that are due to the $3p^5 3d5s$ ($^2P^\circ_{1/2,3/2}$) and $3p^5 3d5d$ ($^2F^\circ_{5/2,7/2}$) resonances, whereas the total integrated strength of the peak found at 34.6 eV is due to roughly equal contributions from the $3p^5 3d5p$ ($^2P_{1/2,3/2}$, $^2D_{3/2,5/2}$, and $^2S_{1/2}$) resonances.

It is seen in Fig. 9 that our computed rate coefficient spectrum agrees reasonably well with the TSR measurements [24], and equally well with the stronger resonances from the VSS measurements [13]. On the other hand, for certain collision energies, the computed resonant strength may differ from experimental findings by as much as a factor of 2. Such a discrepancy was discussed earlier in Sec. IV A where the $3p^5 3d^2$ ($^2D^\circ_{5/2}$) resonance at 4.272 eV had roughly twice the strength. A second large discrepancy is found at 29.8 eV, where the combined strength of the dominant $3p^5 3d4d$ ($^2F^\circ_{5/2,7/2}$) resonances constitutes only one third of the measured strength. Including nearby overlapping resonances reduces this difference to a factor of $\frac{1}{2}$. Another example of

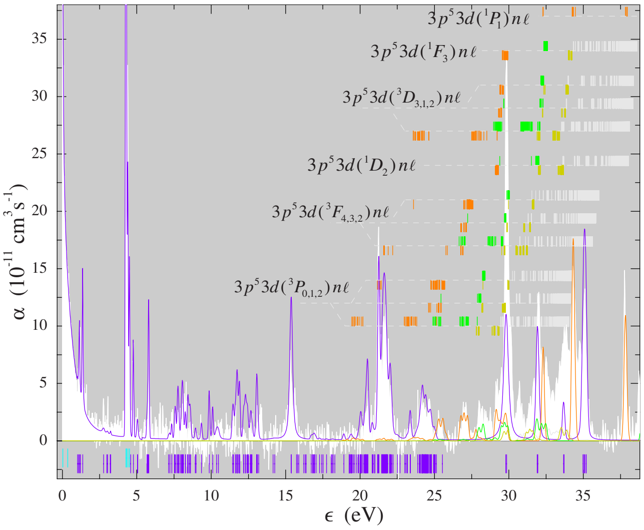

FIG. 9. (Color online) Overview of Ti^{4+} rate coefficient spectra for intermediate energies containing Rydberg series of resonances converging to $3p^53d$ core excitation thresholds. Color codes used for the field-free results are as follows: cyan, $n=3$; blue, $n=4$; red, $n=5$; green, $n=6$; yellow, $n=7$; gray, $n\geqslant 8$; white area, TSR experiment [24].

computed resonance strengths being weaker than experimentally observed ones is seen in the vicinity of the $3p^53d(^3P^{\circ}_{0,1,2})$ thresholds. This discrepancy could be attributed to too small a value (4.85 $\mu\mathrm{s}^{-1}$) for the $3p^53d\ (^3P^{\circ}_1) \rightarrow 3p^6\ (^1S_0)$ radiative rate, despite reasonable agreement with other computed and experimental data [68] as shown in Table II.

C. Dominant Rydberg series Region

Most of the measured DR strength in Fig. 10 is found in the energy region 42–50 eV and is due to resonance series associated with the dominant

$$e^- + 3p^6(^1S_0) \rightarrow 3p^53d(^1P^{\circ}_1)n\ell \rightarrow 3p^6n\ell$$

dipole-allowed core excitation. Here these higher-lying n members are affected by motional electric fields inside the storage-ring bending magnets, as discussed in Sec. IV C 1.

It is important to emphasize that the computed field-free DR rate coefficient in Fig. 10 is on average 35% higher than the experimental rate coefficient in the 42–48 eV range, and about four times larger at the peak height at 49 eV. This discrepancy is mostly removed by inclusion of the subtle field ionization of loosely bound Rydberg states in the recombined Ti^{3+} ion. Specifically, good agreement with the experiment is achieved through a modeling of the theoretical curve by modifying the field-free cross section by the computed survival probability. Modeling of the survival probability of the $3p^6n\ell$ recombined states, due to the possibility of field ionization, is now described.

1. External field effects

It is a common assumption in Eq. (1) that, upon the completion of the two-step DR process, the newly formed

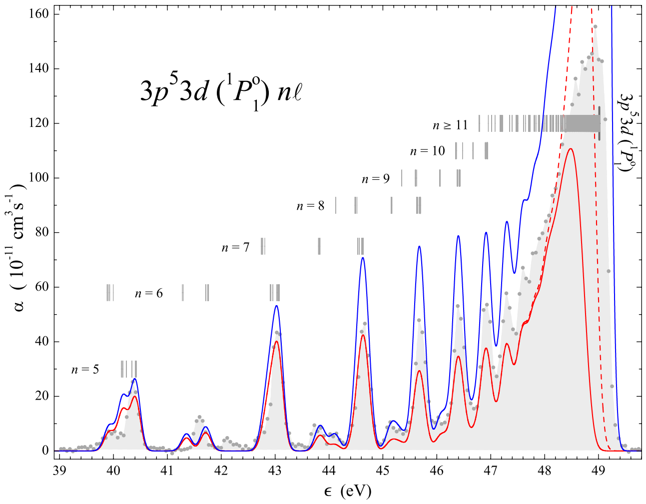

FIG. 10. (Color online) Ti^{4+} rate coefficient, consisting of the dominant Rydberg states converging to $3p^53d(^1P^o_1)$ limit: gray area, experiment [24]; blue curve, field-free MCBP results; dashed red curve, results incorporating motional field effects via a perturbed hydrogenic approximation, and only considering single radiative transitions; solid red curve, results also including full radiative cascade.

Rydberg states $\mathrm{Ti}^{3+*}(3p^6n\ell)$ will radiatively decay into energetically lower states before these recombined ions enter the charge-state-analyzing dipole (CSAD) magnet. This assumption is valid only for Rydberg states having radiative cascading lifetimes less than a flight time $\tau_f=422$ ns [24]. Field-ionization effects in the CSAD magnet strongly depend on the atomic properties of Rydberg states in the presence of a motional electric field $\vec{\mathcal{F}}$. Taking into account radiative decay of Rydberg states during a flight time τ_f, it was suggested that the survival probability $P(n)$ should be a simple step function [24]:

$$P(n) = \begin{cases} 1 & n \leqslant n_{\mathrm{cut}} = 30 \\ 0 & n > n_{\mathrm{cut}} = 30 \end{cases} .$$

This is based on the semiclassical approximation that the maximum height of the total potential $V(r)=-Z/r - \mathcal{F}r\cos\theta$ on the downhill region $\theta=0$ defines the cutoff principle quantum number n_{cut}:

$$V_{max} = -2\sqrt{Z\mathcal{F}} = -Z^2/2n^2_{\mathrm{cut}}.$$

However, in order to reproduce the actual TSR spectra, a nonzero survival probability for $n<200$ states had to be allowed. Based on the maximum magnetic rigidity (1.5 Tm) of the TSR CSAD magnets and the imposed limit of 600 keV/amu on the energy of the Ti^{4+} beam [24], we can expect the maximum field strength in the CSAD magnet to be $\mathcal{F}_{\mathrm{max}} \approx 3.2\times 10^{-6}$ a.u. Based on these experimental findings, we now describe the basic modeling of field ionization effects.

Depending on the strength of the external motional electric field $\mathcal{F}$, hydrogenic levels split into upshifted $(n_1>n_2)$ and downshifted $(n_2>n_1)$ sublevels that correspond to blue and red Stark states, respectively, each with energy

$E(n_1,n_2,|m|;\xi)$ and width $\Gamma(n_1,n_2,|m|;\xi)$ described by parabolic quantum numbers n_1, n_2 and the absolute value of the magnetic quantum number m [62]. Additional dependence on external field strength is usually introduced through the parameter $\xi=n^3\mathcal{F}/4Z_*^3$, where $n=n_1+n_2+|m|+1$ is the principal quantum number and Z_* is the effective nuclear charge. The bound portion of the electronic wave functions in the presence of an external field is described by a good quantum number n_1, and, for energies well below the classical ionization limit, $V_{\max}$, also by the quantum number n_2. However, for energies just below $V_{\max}$, the eigenspectrum contains resonances with tunneling ionization rates that vary rapidly with n_2 [105], so that blue Stark states require stronger fields for ionization than red Stark states.

In contrast to hydrogenic systems, the field-free problem of hydrogenlike ions is not separable in parabolic coordinates due to the finite ionic core giving a non-Coulombic potential inside the ionic-core charge cloud (equivalently, the quantum defect is nonzero, see Ref. [106], p. 87). Consequently, n_1 is only an approximate quantum number and the zero-field energies correspond to spin-orbit coupled $n\ell sjm_j$ eigenstates. Bound states of high n_1, with low autoionization rates that are exponentially dependent on the field strength, become coupled to lower-n resonances above the Stark-split continua (see Ref. [106], Fig. 6.18), acquiring much stronger autoionization rates. In addition, within each symmetry block m_j, the interaction among high n_1 states at avoided crossings will result in a redistribution of autoionization rates [107].

The evolution of $\mathrm{Ti}^{3+*}(3p^6n\ell)$ Rydberg states in the present work is analyzed with the help of Stark maps, constructed for every symmetry block m_j by means of the complex resonance spectrum, $E(n_1,n_2;\xi)-\imath\Gamma(n_1,n_2;\xi)/2$. The imaginary part of the complex resonance energy is used to infer the survival probability $P(n,\mathcal{F})$ of the Rydberg manifold n for a given external field strength $\mathcal{F}$. Our approach in computing the average survival probabilities $P(n)$ is based on the method introduced for DR of Mg^+ [108], and previously used for DR of Be^+ ions [109], with several modifications. First, the hydrogenic field-ionization lifetimes $\tau(n_1,n_2,m;\mathcal{F})$ of Damburg and Kolosov [110] are replaced by the values of Hoe *et al.* [111] that give field-ionization rates $\Gamma(\xi)$ in terms of the energies $E(\xi)$ of hydrogenic Stark levels and are more accurate for high-n manifolds. Second, computation of the Stark maps is based on direct diagonalization of the energy matrix

$$H_{nn'}(\mathcal{F})=\delta_{n,n'}E_n^0+\langle n'|\vec{\mathcal{F}}\cdot\vec{r}|n\rangle, \qquad (16)$$

where the zero-field energies E_n^0 are the MCBP eigenenergies described in Sec. II B. We use our values to determine the state-resolved effective nuclear charges Z_* that enter into the screened hydrogenic wave functions $|n\rangle$ used to represent the $n\leqslant 200$ potassiumlike $\mathrm{Ti}^{3+*}(3p^6n\ell)$ states.

In the evaluation of the field-dependent perturbation matrix elements in Eq. (16), for increasing field strengths in steps of 160 V/cm up to $\mathcal{F}_{\max}$, we have used the closed-form results of Ref. [112]. Each energy level in the generated Stark maps is traced through numerous (avoided) crossings to the classical ionization limit V_{sp}, which is valid for hydrogenic Stark states belonging to $m=0$ symmetry (see Ref. [106], p. 83). Hydrogenic Stark states of $m\neq 0$ symmetry have the first ionization threshold at slightly higher energies [113], as recently discussed by Menéndez *et al.* for potassium atoms [114]. This small increase of the classical ionization limit will result in nonvanishing survival probabilities, $P(n,\mathcal{F}_{\max})>0$, even for $n\geqslant 34$ manifolds.

In the experimental environment, the behavior of $P(n)$, as it varies from unity for low n to zero for high n, depends on the population distribution of $\mathrm{Ti}^{3+*}(3p^6n\ell)$ states at the moment they enter the CSAD magnet. In order to compare our field-free computed results to the experimental results, we scaled our computed results according to

$$\alpha^{\text{field}}(\epsilon)=\sum_n P(n)\alpha_n^{\text{field-free}}(\epsilon). \qquad (17)$$

Our field-free MCBP calculations for the radiative transition rates of high-n Rydberg states indicate that the dominant $n\ell\to n'\ell'$ radiative decay path involves the $\ell=n-1$ and $\ell'=n'-1=n-2$ states. The field-free relaxation times $\tau_{\min}$ along this path can be summarized in the following form:

$$\tau_{\min}[\mathrm{ns}]\approx\begin{cases}(0.548/Z_*)^4n^5 & \text{single transition}\\(0.358/Z_*)^4n^6 & \text{full cascade,}\end{cases} \qquad (18)$$

which in turn implies that during the flight time τ_f only $n\leqslant 14$ Rydberg states will cascade to the ground state before entering the CSAD magnet. It is important to note that before reaching the CSAD magnet, the recombined ions pass through (i) the toroidal magnet used for deflecting the electron beam out of the ion's beam path, (ii) the correction dipole magnet, and (iii) the focusing (quadrupole) magnets. As a result, due to intramanifold (same n, different ℓ) field-induced level mixing, we can expect a considerable reduction in radiative lifetimes of the majority of high-ℓ states within the $n>45$ manifolds, and a significant shortening of their stabilization times before entering the CSAD magnet. Such field-induced radiative decay (known as "delayed cutoff") is responsible for a small but nonzero contribution of high-n DR resonances far beyond the "hard cutoff" $n_{\max}$ [24], and has been previously observed as well (see, for example, Refs. [115–117]). Modeling of the delayed cutoff is beyond the scope of the present work as it requires detailed knowledge of the experimental setup [118]; here we instead assume that the average survival probability $P(n)$ of $50\leqslant n\leqslant 200$ manifolds is 0.16, where we adopted 1:3:39 ratios for the magnetic flux densities in toroid, correction, and CSAD magnets, respectively [109].

So far we have exploited the fact that potassiumlike $\mathrm{Ti}^{3+*}(3p^6n\ell)$ Rydberg states can be represented sensibly within an independent-particle approximation. However, since the first classification of "an extraneous ${}^2F^\circ_{5/2}$ level" of the $3p^53d^2$ configuration by Swensson and Edlén [7], the atomic structure of Ti^{3+} has received considerable experimental and theoretical attention, due in large part to the existence of 39 bound and six autoionizing $\mathrm{Ti}^{3+**}(3p^53d^2)$ doubly excited, strong ($3p\to 3d$ core transition) resonances.

In our MCBP calculations, the strongest zero-field perturbation of Rydberg series converging to the first ionization

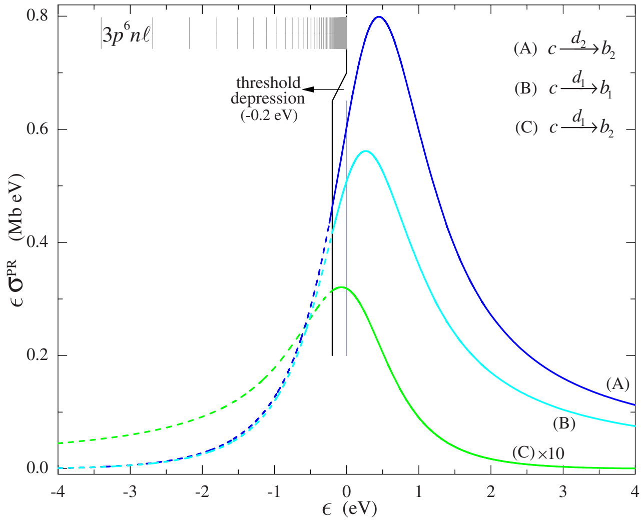

FIG. 11. (Color online) Partial PR contributions using Eq. (12) and continued below threshold, showing the overlap of the $3p^5 3d^2(^2F)$ resonances with the $3p^6 n\ell$ recombined Rydberg states, giving rise to "forced autoionization."

limit is the appreciable mixing of the $3p^6 nf(^2F^\circ)$ and $3p^5 3d^2(^2F^\circ)$ states (see also Ref. [14], p. 2219). For example, the admixture of the $3p^5 3d^2$ bound-levels peaks at 22% and 8% for the two $3p^6 5f$ states, respectively. Although less than 1% for $3p^6 nf n \geqslant 6$ states, even weak mixing leads to an enhanced autoionization rate due to the much larger $3p^5 3d^2$ autoionization transition matrix element. Thus the motional electric field in the CSAD magnet may give rise to a so called "forced autoionization" phenomenon (see Ref. [106], p. 461, and Fig. 11).

For the present case, all $n \geqslant 34$ Rydberg manifolds will open up directly to Stark induced continua and, more importantly, will undergo forced autoionization through coupling with the $3p^5 3d^2(^2F^\circ_{5/2,7/2})$ resonances. Our computed "forced" autoionization rates (in ns^{-1}) for $3p^6 n\ell$ states, where $n \geqslant (Z_*^3/16\mathcal{F})^{1/4}$, are as follows:

$$A^a \approx \left\{ \begin{array}{lll} {}^2S: & 4.91^{[+5]}_{(3)} n^{-3}; & {}^2P^\circ: 1.21^{[+6]}_{(1)} n^{-3} \\ {}^2F^\circ_{5/2}: & 1.50^{[+7]}_{(5)} n^{-3/2}; & {}^2D: 1.78^{[+7]}_{(1)} n^{-3} \\ {}^2F^\circ_{7/2}: & 1.74^{[+8]}_{(5)} n^{-5/2}; & {}^2G: 1.7^{[+4]}_{(1)} n^{-3} \\ \text{else:} & 0; & {}^2H^\circ: 8.5^{[+0]}_{(1)} n^{-3} \end{array} \right\} \qquad (19)$$

with numbers in parentheses and square brackets being fitting uncertainties and powers of ten, respectfully.

The departure of autoionization rates in Eq. (19) from n^{-3} scaling for the $3p^6 nf$ levels stems from small admixtures of the $3p^5 3d^2(^2F^\circ_{5/2,7/2})$ levels, which can be expressed for all $n \geqslant (Z_*^3/16\mathcal{F})^{1/4}$ Rydberg manifolds as

$$|\langle 3p^6 nf | d_{1,2}\rangle|^2 \approx \left\{ \begin{array}{l} d_1: 2.6(1) n^{-3/2} \\ d_2: 30(1) n^{-5/2} \end{array} \right\}. \qquad (20)$$

Through intermanifold mixing induced by the external field $\mathcal{F}$, we can also expect $n < 34$ Rydberg manifolds to inherit the weak autoionizing character especially in the vicinity of perturbing $3p^5 3d^2(^2F^\circ)$ bound states. In order to assess qualitatively the spread of Stark induced autoionization rates in each symmetry block m_j, we use a complex scaling approach in evaluating the field-dependent perturbation term in Eq. (16).

The complex scaling technique has been extensively used to treat resonant phenomena in atomic and molecular physics [119] and chemistry, as reviewed by Moiseyev [120]. Its novel implementations are found in diverse fields, such as investigation of the properties of shallow quantum wells in the regime of strong quantum confinement [121], or evaluation of leaky modes for various resonating structures in wave guides [122]. The mathematical foundation of complex scaling, within the theory of dilatation analyticity for Coulombic systems, has been described by Combes and co-workers [123,124] and by Simon [125], the main result being that, under the interior scaling transformation $r \to r\exp(\imath\vartheta)$, bound states of the original (real) Hamiltonian remain unaffected while the continuous spectrum rotates in the complex plane. This rotation reveals so-called "hidden" complex eigenvalues of the transformed Hamiltonian that are stabilized with respect to changes in the transformation parameter ϑ.

Extension of the complex scaling method to Stark systems [126–129], where the potential does not vanish at infinity, is applicable only for $\vartheta < \pi/3$, which limits not only the resonance widths and positions but also the strength $\mathcal{F}$ of electric fields that can be treated by this method. Our modeling of the joint evolution of the $3p^5 3d^2$ states and the $n \leqslant 50$ Rydberg states in weak fields ($\xi < 0.002$) relies on direct diagonalization of the Hamiltonian in Eq. (16) in its complex-scaled form,

$$H_{nn'}(\mathcal{F};\vartheta) = \delta_{n,n'} E_n^0 + \langle n'_{(\vartheta)} | \vec{\mathcal{F}} \cdot \vec{r} | n_{(\vartheta)} \rangle, \qquad (21)$$

using the following approximations. First, all $3p^6 n\ell$ and $3p^5 3d^2$ states were represented by screened, complex-rotated hydrogenic wave functions $|n_{(\vartheta)}\rangle$. Second, the (field-dependent) imaginary part of the diagonal elements of the perturbation matrix were replaced by values found in Eq. (19) and Table V, since the two near-threshold $3p^5 3d^2(^2F^\circ_{5/2,7/2})$ resonances are too broad to satisfy the requirement $\vartheta < \pi/3$. Third, stationarity of the (complex) eigenvalues has been confirmed for several values (5°, 10°, and 15°) of the transformation parameter ϑ.

Interpreting the imaginary part of the complex eigenvalues as the "forced" autoionization rates, we compute the average survival probabilities $P(n)$ of the $3p^6 n\ell$ states in the CSAD magnet. The dwell time of the $\mathrm{Ti}^{3+*}(3p^6 n\ell)$ Rydberg states in the CSAD magnet is taken to be 100 ns with an average slew rate of 292×10^9 V/cm s.

Our computed survival probabilities, at various levels of sophistication, are shown in Fig. 12, as well as the inferred probability. A comparison between results with and without the inclusion of the $3p^5 3d^2$ perturbers indicates that a significant modification of survival probability exists for principal quantum number as low as $n = 6$. While we have reproduced theoretically the qualitative feature of the inferred survival probability, there is quantitative disagreement that we assess to be due to additional experimental environmental condi-

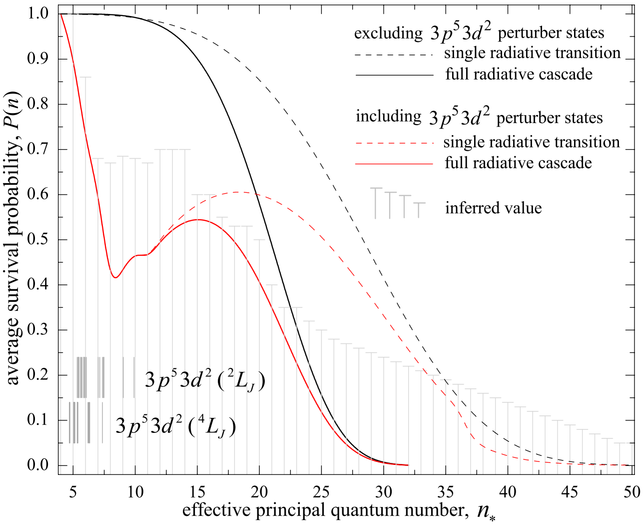

FIG. 12. (Color online) Computed survival probability, $P(n)$, with and without inclusion of the $3p^5 3d^2$ perturbers, and the inferred probability, $P^{\mathrm{inf}}(n)$, required to match the experiment above 43 eV (see Eq. (17) and Fig. 10).

tions not taken into account here and/or inaccuracies due to our hydrogenic approximation. Nevertheless, the general behavior of either probability curve indicates that field ionization effects are prominent throughout the Rydberg series, and furthermore, that forced autoionization due to $3p^5 3d^2$ perturber states is important.

V. SUMMARY AND CONCLUSION

In our study of argonlike Ti^{4+} PR, we have found that the broad, highly correlated, threshold-straddling, asymmetric $3p^5 3d^2 (^2F^{\circ}_{5/2,7/2})$ resonances play a distinct role. At low incident-electron energies, the threshold PR behavior is dominated by those two resonances that only contribute partially to the total Maxwellian rate coefficient, due to their straddling of threshold. Further, there is noticeable asymmetry in the resulting resonance profile that can be observed experimentally at TSR via PR measurements and at ALS via PI measurements. Theoretical modeling of the resultant Fano profile was performed including higher-order resonant-direct (DR/RR) interference effects, and was found to quantify the asymmetry behavior, in good agreement with ALS PI results.

At higher incident-electron energies, as the excited thresholds give rise to the dominant $3p^5 3dn\ell$ Rydberg series of resonances, we find that the recombined series $3p^6 n\ell$ are strongly perturbed by the below-threshold tail of those same $3p^5 3d^2 (^2F^{\circ})$ states. This leads to forced autoionization and a reduction in the experimentally observed DR strength. The reduction factor is the survival probability of recombined Rydberg states against reionization due to field effects and can be modeled qualitatively by a hydrogenic, perturbed Rydberg series approach.

In conclusion, we find that higher-order correlation, interference effects for broad resonances, and field ionization effects, in order to reproduce observation, need to be considered for a proper treatment of PR in argonlike Ti^{4+}. We have performed similar calculations for computing the PR rate coefficients for the remainder of the argonlike isoelectronic sequence, and will be presenting this astrophysically important data in future publications.

ACKNOWLEDGMENTS

This work was supported in part by NASA APRA and SHP SR&T programs. We thank S. Schippers for supplying the experimental data in numerical form and for helpful comments. We also thank A. E. Kingston for providing the CIV3 radial functions for comparative purposes.

---

[1] R. K. Janev, Phys. Scr. **T37**, 5 (1991).
[2] Y. Mochizuki, K. Takahashi, H. T. Janka, W. Hillebrandt, and R. Diehl, Astron. Astrophys. **346**, 831 (1999).
[3] H. N. Russell and R. J. Lang, Astrophys. J. **66**, 13 (1927).
[4] P. G. Kruger and S. G. Weissberg, Phys. Rev. **48**, 659 (1935).
[5] L. Å. Svensson and J. O. Ekberg, Ark. Fys. **37**, 65 (1968).
[6] L. Å. Svensson and J. O. Ekberg, Ark. Fys. **40**, 145 (1969).
[7] J. W. Swensson and B. Edlén, Phys. Scr. **9**, 335 (1974).
[8] B. Edlén and J. W. Swensson, Phys. Scr. **12**, 21 (1975).
[9] L. Å. Svensson, Phys. Scr. **13**, 235 (1976).
[10] A. N. Ryabtsev, Nucl. Instrum. Methods Phys. Res. B **31**, 196 (1988).
[11] G. Duffy, J. Phys. B **35**, L119 (2002).
[12] S. Schippers *et al.*, J. Phys. B **37**, L209 (2004).
[13] A. N. Ryabtsev, S. S. Churilov, and E. Y. Kononov, Opt. Spectrosc. **98**, 519 (2005).
[14] A. E. Kingston and A. Hibbert, J. Phys. B **39**, 2217 (2006).
[15] A. E. Kingston and A. Hibbert, J. Phys. B **41**, 155001 (2008).
[16] R. A. Falk, G. H. Dunn, D. C. Griffin, C. Bottcher, D. C. Gregory, D. H. Crandall, and M. S. Pindzola, Phys. Rev. Lett. **47**, 494 (1981).
[17] D. C. Griffin, C. Bottcher, and M. S. Pindzola, Phys. Rev. A **25**, 1374 (1982).
[18] R. A. Falk, G. H. Dunn, D. C. Gregory, and D. H. Crandall, Phys. Rev. A **27**, 762 (1983).
[19] D. W. Mueller, T. J. Morgan, G. H. Dunn, D. C. Gregory, and D. H. Crandall, Phys. Rev. A **31**, 2905 (1985).
[20] S. J. Chantrenne, D. C. Gregory, M. J. Buie, and M. S. Pindzola, Phys. Rev. A **41**, 140 (1990).
[21] T. W. Gorczyca, M. S. Pindzola, D. C. Griffin, and N. R. Badnell, J. Phys. B **27**, 2399 (1994).
[22] U. Hartenfeller, K. Aichele, D. Hathiramani, G. Hofmann, V. Schäfer, M. Steidl, M. Stenke, E. Salzborn, and M. S. Pindzola, J. Phys. B **31**, 2999 (1998).
[23] U. Hartenfeller, K. Aichele, D. Hathiramani, V. Schäfer, M. Steidl, F. Scheuermann, and E. Salzborn, J. Phys. B **31**, 3013 (1998).
[24] S. Schippers, T. Bartsch, C. Brandau, G. Gwinner, J. Linke-

mann, A. Müller, A. A. Saghiri, and A. Wolf, J. Phys. B **31**, 4873 (1998).

[25] D. B. Popović *et al.*, Phys. Rev. A **65**, 034704 (2002).

[26] T. v. Zoest, H. Knopp, J. Jacobi, S. Schippers, R. A. Phaneuf, and A. Müller, J. Phys. B **37**, 4387 (2004).

[27] M. Martins, K. Godehusen, T. Richter, P. Wernet, and P. Zimmermann, J. Phys. B **39**, R79 (2006).

[28] J. E. Hansen, H. Kjeldsen, F. Folkmann, M. Martins, and J. B. West, J. Phys. B **40**, 293 (2007).

[29] R. Schuch, E. Lindroth, S. Madzunkov, M. Fogle, T. Mohamed, and P. Indelicato, Phys. Rev. Lett. **95**, 183003 (2005).

[30] E. W. Schmidt *et al.*, Astrophys. J. Lett. **641**, L157 (2006).

[31] N. R. Badnell, M. G. O'Mullane, H. P. Summers, Z. Altun, M. A. Bautista, J. Colgan, T. W. Gorczyca, D. M. Mitnik, M. S. Pindzola, and O. Zatsarinny, Astron. Astrophys. **406**, 1151 (2003).

[32] O. Zatsarinny, T. W. Gorczyca, K. T. Korista, N. R. Badnell, and D. W. Savin, Astron. Astrophys. **412**, 587 (2003).

[33] J. Colgan, M. S. Pindzola, A. D. Whiteford, and N. R. Badnell, Astron. Astrophys. **412**, 597 (2003).

[34] O. Zatsarinny, T. W. Gorczyca, K. T. Korista, N. R. Badnell, and D. W. Savin, Astron. Astrophys. **417**, 1173 (2004).

[35] J. Colgan, M. S. Pindzola, and N. R. Badnell, Astron. Astrophys. **417**, 1183 (2004).

[36] Z. Altun, A. Yumak, N. R. Badnell, J. Colgan, and M. S. Pindzola, Astron. Astrophys. **420**, 775 (2004).

[37] O. Zatsarinny, T. W. Gorczyca, K. Korista, N. R. Badnell, and D. W. Savin, Astron. Astrophys. **426**, 699 (2004).

[38] D. M. Mitnik and N. R. Badnell, Astron. Astrophys. **425**, 1153 (2004).

[39] O. Zatsarinny, T. W. Gorczyca, J. Fu, K. T. Korista, N. R. Badnell, and D. W. Savin, Astron. Astrophys. **447**, 379 (2006).

[40] N. R. Badnell, Astron. Astrophys. **447**, 389 (2006).

[41] Z. Altun, A. Yumak, N. R. Badnell, S. D. Loch, and M. S. Pindzola, Astron. Astrophys. **447**, 1165 (2006).

[42] M. A. Bautista and N. R. Badnell, Astron. Astrophys. **466**, 755 (2007).

[43] Z. Altun, A. Yumak, I. Yavuz, N. R. Badnell, S. D. Loch, and M. S. Pindzola, Astron. Astrophys. **474**, 1051 (2007).

[44] N. R. Badnell, J. Phys. B **39**, 4825 (2006).

[45] N. R. Badnell, Astrophys. J. Lett. **651**, L73 (2006).

[46] T. W. Gorczyca, M. S. Pindzola, F. Robicheaux, and N. R. Badnell, Phys. Rev. A **56**, 4742 (1997).

[47] T. W. Gorczyca, N. R. Badnell, F. Robicheaux, and M. S. Pindzola, in *Atomic Processes in Plasmas*, edited by E. Oks and M. S. Pindzola, AIP Conf. Proc. No. 443 (AIP, Woodbury, NY, 1998).

[48] S. Schippers, S. Kieslich, A. Müller, G. Gwinner, M. Schnell, A. Wolf, A. Covington, M. E. Bannister, and L. B. Zhao, Phys. Rev. A **65**, 042723 (2002).

[49] N. R. Badnell, J. Phys. B **19**, 3827 (1986); **30**, 1 (1997).

[50] S. Schippers, T. Bartsch, C. Brandau, J. Linkemann, A. Müller, A. A. Saghiri, and A. Wolf, Hyperfine Interact. **114**, 273 (1998).

[51] S. Schippers, T. Bartsch, C. Brandau, A. Müller, G. Gwinner, J. Linkemann, A. A. Saghiri, and A. Wolf, Phys. Scr. **T80B**, 314 (1999).

[52] S. Schippers *et al.*, Phys. Rev. Lett. **89**, 193002 (2002).

[53] S. Schippers *et al.*, Phys. Rev. A **67**, 032702 (2003).

[54] N. R. Badnell, M. S. Pindzola, and D. C. Griffin, Phys. Rev. A **43**, 2250 (1991).

[55] T. W. Gorczyca, N. R. Badnell, and D. W. Savin, Phys. Rev. A **65**, 062707 (2002).

[56] M. S. Pindzola, F. J. Robicheaux, N. R. Badnell, M. H. Chen, and M. Zimmermann, Phys. Rev. A **52**, 420 (1995).

[57] D. A. Knapp, P. Beiersdorfer, M. H. Chen, J. H. Scofield, and D. Schneider, Phys. Rev. Lett. **74**, 54 (1995).

[58] E. Behar, V. L. Jacobs, J. Oreg, A. Bar-Shalom, and S. L. Haan, Phys. Rev. A **62**, 030501(R) (2000).

[59] M. S. Pindzola, N. R. Badnell, and D. C. Griffin, Phys. Rev. A **46**, 5725 (1992).

[60] M. H. Chen, K. J. Reed, and D. L. Moores, Phys. Rev. Lett. **64**, 1350 (1990).

[61] A. Bar-Shalom, M. Klapisch, and J. Oreg, J. Quant. Spectrosc. Radiat. Transf. **71**, 169 (2001).

[62] E. Merzbacher, *Quantum Mechanics*, 3rd ed. (Wiley, New York, 1998).

[63] D. M. Mitnik, M. S. Pindzola, and N. R. Badnell, Phys. Rev. A **59**, 3592 (1999).

[64] U. Fano, Phys. Rev. **124**, 1866 (1961).

[65] U. Fano and J. W. Cooper, Phys. Rev. **137**, A1364 (1965).

[66] P. Bryans, E. Landi, and D. W. Savin, e-print arXiv:0805.3302v2.

[67] A. Irimia and C. Froese-Fischer, www.vuse.vanderbilt.edu/~cff/mchf_collection

[68] T. Shirai, J. Sugar, A. Musgrove, and W. L. Wiese, J. Phys. Chem. Ref. Data Monogr. **8**, 632 (2000).

[69] A. Burgess, H. E. Manson, and J. A. Tully, Astron. Astrophys. **217**, 319 (1989).

[70] W. Eissner, M. Jones, and H. Nussbaumer, Comput. Phys. Commun. **8**, 270 (1974).

[71] Y. Ralchenko, A. E. Kramida, J. Reader, and NIST ASD Team, NIST Atomic Spectra Database (version 3.1.4), http://physics.nist.gov/asd3

[72] A. Hibbert, Comput. Phys. Commun. **9**, 141 (1975).

[73] M. Lestinsky *et al.*, Phys. Rev. Lett. **100**, 033001 (2008).

[74] S. Madžunkov, E. Lindroth, N. Eklöw, M. Tokman, A. Paál, and R. Schuch, Phys. Rev. A **65**, 032505 (2002).

[75] H. Poth, Phys. Rep. **196**, 135 (1990).

[76] P. F. Dittner, S. Datz, P. D. Miller, P. L. Pepmiller, and C. M. Fou, Phys. Rev. A **33**, 124 (1986).

[77] D. Nikolić, Master's thesis, University of Stockholm, AlbaNova Universitetscentrum, Roslagstullsbacken 21, Stockholm, Sweden, 2003.

[78] R. Piessens and M. Branders, Math. Comput. **28**, 135 (1974).

[79] D. P. Laurie, Math. Comput. **66**, 1133 (1997).

[80] A. Müller, Int. J. Mass. Spectrom. **192**, 9 (1999).

[81] G. Gwinner *et al.*, Phys. Rev. Lett. **84**, 4822 (2000).

[82] M. Hörndl, S. Yoshida, J. Burgdörfer, G. Gwinner, and A. Wolf, Hyperfine Interact. **173**, 67 (2006).

[83] F. Bachari, F. Ferro, G. Maero, and P. Quarati, in *International Symposium on Nuclear Astrophysics—Nuclei in the Cosmos—IX* (ISOLDE and nTOF Team, CERN, Geneva, 2006), p. 167.

[84] Y. G. Tsamis, M. J. Barlow, X. W. Liu, I. J. Danziger, and P. J. Storey, Mon. Not. R. Astron. Soc. **338**, 687 (2003).

[85] Y. Hahn, Phys. Scr. **T37**, 53 (1991).

[86] M. Landini and B. C. M. Fossi, Astron. Astrophys. Suppl. Ser. **91**, 183 (1991).

[87] R. A. Hulse, Nucl. Technol./Fusion **3**, 259 (1983).

[88] P. Mazzotta, G. Mazzitelli, S. Colafrancesco, and N. Vittorio, Astron. Astrophys. Suppl. Ser. **133**, 403 (1998).

[89] Y. Hahn, J. Quant. Spectrosc. Radiat. Transf. **41**, 315 (1989).

[90] A. Burgess, Astrophys. J. **141**, 1588 (1965).

[91] R. Mewe, J. Schrijver, and J. Sylwester, Astron. Astrophys. Suppl. Ser. **40**, 323 (1980).

[92] V. L. Jacobs, J. Davis, P. C. Kepple, and M. Blaha, Astrophys. J. **211**, 605 (1977).

[93] S. M. R. Ansari, G. Elwert, and P. Mücklich, Z. Naturforsch. A **25A**, 1781 (1970).

[94] N. R. Badnell, Astrophys. J., Suppl. Ser. **167**, 334 (2006).

[95] D. A. Verner and G. J. Ferland, Astrophys. J., Suppl. Ser. **103**, 467 (1996).

[96] M. F. Gu, Astrophys. J. **589**, 1085 (2003).

[97] K. T. Korista (private communication).

[98] P. G. Burke and W. D. Robb, Adv. At. Mol. Phys. **11**, 143 (1976).

[99] P. G. Burke and K. A. Berrington, *Atomic Molecular Processes: An R-matrix Approach* (IOP Publishing, Bristol, 1993).

[100] F. Robicheaux, T. W. Gorczyca, M. S. Pindzola, and N. R. Badnell, Phys. Rev. A **52**, 1319 (1995).

[101] T. W. Gorczyca, F. Robicheaux, M. S. Pindzola, and N. R. Badnell, Phys. Rev. A **52**, 3852 (1995).

[102] T. W. Gorczyca, F. Robicheaux, M. S. Pindzola, and N. R. Badnell, Phys. Rev. A **54**, 2107 (1996).

[103] A. M. Sossah, H. L. Zhou, and S. T. Manson, Bull. Am. Phys. Soc. **58**, 36 (2008).

[104] S. T. Manson (private communication).

[105] L. D. Landau and L. M. Lifshitz, *Quantum Mechanics: Non-Relativistic Theory*, 3rd ed. (Butterworth-Heinemann, Burlington, MA, 1981), Vol. 3, p. 295.

[106] T. F. Gallagher, *Rydberg Atoms* (Cambridge University Press, London, 1994).

[107] J. Y. Liu, P. McNicholl, D. A. Harmin, J. Ivri, T. Bergeman, and H. J. Metcalf, Phys. Rev. Lett. **55**, 189 (1985).

[108] A. Müller, D. S. Belić, B. D. DePaola, N. Djurić, G. H. Dunn, D. W. Mueller, and C. Timmer, Phys. Rev. A **36**, 599 (1987).

[109] T. Mohamed, D. Nikolić, E. Lindroth, S. Madžunkov, M. Fogle, M. Tokman, and R. Schuch, Phys. Rev. A **66**, 022719 (2002).

[110] R. J. Damburg and V. V. Kolosov, J. Phys. B **12**, 2637 (1979).

[111] N. Hoe, B. D'Etat, J. Grumberg, M. Caby, E. Leboucher, and G. Coulaud, Phys. Rev. A **25**, 891 (1982).

[112] M. Bautista-Moedano and J. L. López-Bonilla, Apeiron **13**, 34 (2006).

[113] W. E. Cooke and T. F. Gallagher, Phys. Rev. A **17**, 1226 (1978).

[114] J. M. Menéndez, I. Martín, and A. M. Velasco, Theor. Chem. Acc. **115**, 65 (2006).

[115] D. R. DeWitt, R. Schuch, T. Quinteros, H. Gao, W. Zong, H. Danared, M. Pajek, and N. R. Badnell, Phys. Rev. A **50**, 1257 (1994).

[116] D. R. DeWitt, E. Lindroth, R. Schuch, H. Gao, T. Quinteros, and W. Zong, J. Phys. B **28**, L147 (1995).

[117] W. Zong, R. Schuch, E. Lindroth, H. Gao, D. R. DeWitt, S. Asp, and H. Danared, Phys. Rev. A **56**, 386 (1997).

[118] S. Schippers, A. Müller, G. Gwinner, J. Linkemann, A. A. Saghiri, and A. Wolf, Astrophys. J. **555**, 1027 (2001).

[119] W. Reinhardt, in *Spectral Theory and Mathematical Physics: A Festschrift in Honor of Barry Simon's 60th Birthday*, Proceedings of Symposia in Pure Mathematics, Vol. 76, edited by F. Gesztesy, P. Deift, C. Galvez, P. Perry, and W. Schlag (AMS, Providence, 2007), pp. 357–382.

[120] N. Moiseyev, Phys. Rep. **302**, 212 (1998).

[121] L. I. Deych and I. V. Ponomarev, Phys. Rev. B **71**, 035342 (2005).

[122] S. Hein, T. Hohage, and W. Koch, J. Fluid Mech. **506**, 255 (2004).

[123] J. Aguilar and J. M. Combes, Commun. Math. Phys. **22**, 269 (1971).

[124] E. Balslev and J. M. Combes, Commun. Math. Phys. **22**, 280 (1971).

[125] B. Simon, Ann. Math. **97**, 247 (1973).

[126] I. W. Herbst and B. Simon, Phys. Rev. Lett. **41**, 67 (1978).

[127] I. W. Herbst, Commun. Math. Phys. **64**, 279 (1979).

[128] I. W. Herbst, Commun. Math. Phys. **75**, 197 (1980).

[129] I. W. Herbst and B. Simon, Commun. Math. Phys. **80**, 181 (1981).